MULTI-SUBCARRIER SIGNAL PROCESSING FOR FIBER OPTIC COMMUNICATION SYSTEMS

MULTI-SUBCARRIER SIGNAL PROCESSING FOR FIBER OPTIC COMMUNICATION SYSTEMS

BY

RYAN RAMDIAL, B.ENG.

AUGUST 2020

A THESIS

SUBMITTED TO THE DEPARTMENT OF ELECTRICAL & COMPUTER ENGINEERING

AND THE SCHOOL OF GRADUATE STUDIES

IN PARTIAL FULFILMENT OF THE REQUIREMENTS

FOR THE DEGREE OF

MASTER OF APPLIED SCIENCE

MCMASTER UNIVERSITY

MASTER OF APPLIED SCIENCE (2020) McMaster University

Electrical and Computer Engineering Hamilton, ON, Canada

TITLE: Multi-Subcarrier Signal Processing for Fiber Optic Communication Systems

AUTHOR: Ryan Ramdial

B.Eng.

McMaster University, Hamilton, ON, Canada

SUPERVISOR: Dr. Shiva Kumar

NUMBER OF PAGES: xi, 71

Abstract

Although fiber optic communication systems have enjoyed tremendous developments since their inception roughly fifty years ago, there are still improvements to be made. One such area for growth, relating more to long-haul applications of optical fibers, is the mitigation of nonlinear penalties. These nonlinear penalties appear due to the transmitted signal affecting the material properties of the fiber itself, and are more prominent when said signal has more energy in it—a conflicting effect from the traditional stance where more energy is considered beneficial. These penalties come in different forms, although they all have the same degrading effects for the system in question. Therefore, it is imperative to find new techniques that can mitigate these nonlinear penalties to ensure the optimal performance for our systems. One such technique, that we call multi-subcarrier processing, is the interest of the thesis here.

The first section proposes a new method to compensate for the receiver side digital signal processing. More specifically, it introduces an algorithm that can remove the intermediate frequency offset that the signal acquires after passing through the system, which is necessary for coherent systems employed today. As some traditional algorithms used in the signal processing no longer work for multi-subcarrier systems, this new algorithm is necessary to compensate effectively for said offset.

The second section introduces a new signal processing technique for the multiplexing and demultiplexing of multi-subcarrier signals. By making use of the well-known Fast Fourier Transform algorithm, the computational cost for generating said signals can be drastically reduced as the number of subcarriers grow larger. As systems continue the trend of operating at greater baud rates, the savings introduced here should be of even greater significance for commercial systems of the future.

Acknowledgements

I would like to thank Dr. Kumar for the opportunity.

I would also like to thank my parents for their support throughout the years.

Contents

List of Figures

List of Tables

List of Abbreviations

AWGN	**Additive White Gaussian Noise**
ASE	**Amplified Spontaneous Emission**
BER	**Bit Error Rate**
CDC	**Chromatic Dispersion Compensation**
CPB	**Cost-Per-Bit**
DBP	**Digital Back Propagation**
DFT	**Discrete Fourier Transform**
DSP	**Digital Signal Processing**
EDFA	**Erbium-Doped Fiber Amplifier**
EGN	**Enhanced Gaussian Noise**
FFT	**Fast Fourier Transform**
FON	**Fourth-Order Noise**
FWM	**Four-Wave Mixing**
GN	**Gaussian Noise**
IFO	**Intermediate Frequency Offset**
LO	**Local Oscillator**
MMF	**Multi-Mode Fiber**
MSC	**Multi-Subcarrier**
NA	**Numerical Aperture**
NLI	**Nonlinear Interference**

NLSE	**Nonlinear Schrödinger Equation**
OFDM	**Orthogonal Frequency Division Multiplexing**
PDM	**Polarization Division Multiplexing**
PSD	**Power Spectral Density**
RRC	**Root-Raised Cosine**
QPSK	**Quadrature Phase-Shift Keying**
SC	**Single-Carrier**
SMF	**Single-Mode Fiber**
SNR	**Signal-to-Noise Ratio**
SPM	**Self-Phase Modulation**
TIR	**Total Internal Reflection**
WDM	**Wavelength Division Multiplexing**
XC	**Cross-correlation**
XPM	**Cross-Phase Modulation**

Chapter 1

Introduction

Until the 1970s, the traditional method for transmitting information over communication channels was done via either copper cables or free space. However, due to the high losses in these two mediums, a more efficient means was needed for transmitting data at ever-increasing distances. With a growing worldwide population that desired to be more connected, the need for a material that could transport vast amounts of data quickly was required as well. With these two driving forces, optical fibers came into play to meet these demands.

In 1965, Charles K. Kao and George A. Hockman of the Standard Telephones and Cable company were the first to propose that the attenuation in optical fibers could be reduced to 20 dB/km, or less [1]. Though this parameter was still in the range of copper cables such as twisted pair wires, the much greater bandwidth that optical fibers brought due to utilizing a higher carrier frequency proved that they could indeed be a viable medium for communications systems. Furthermore, through the manufacturing process of the fiber and removing some "impurities", they also proposed that the attenuation could be reduced even further.

Up until the end of the next decade (and still continuing to this day), there was much work done to reduce the attenuation as much as possible. This led to the discovery of a first operating point, or "window", centered at 850 nm, followed by a second window at 1300 nm. However, it was in 1979 when a third window at 1550 nm was discovered which had a loss of ~0.2 dB/km [2]. This point of operation was such a breakthrough that it remains the optimal choice for transmitting information on fibers to this day. With another recent development—distributed feedback lasers—at that time as well, optical fibers were almost ready to take over the telecommunications industry. However, it was until the success of two other key technologies that finally enabled it to do so.

The first of these was the optical amplifier—more specifically the erbium-doped fiber amplifier (EDFA)—developed during the mid-1980s. Prior to optical amplifiers, the transmitted signal had to be converted back to the electrical domain after every span of fiber to regain the lost power, and then was reconverted back to the optical domain for further transmission. This optical-electrical-optical conversion (O.E.O.) process was very expensive and made transmitting signals at large distances unfeasible from a commercial standpoint. With the advent of the optical amplifier, the costs associated with regeneration of the signal decreased significantly, making low-cost, long-distance transmission one-step closer to becoming a reality.

The second of these developments, though not a new concept, was the creation of the technology that allowed the application of wavelength-division multiplexing (WDM) to fiber optic systems. Before this, a single fiber had to be dedicated for each signal that was to be transmitted—a very inefficient and impractical goal. WDM technology instead allowed multiple signals to share the same fiber, reducing the total system cost per transmitted bit drastically by making full use of the large bandwidth optical fibers enjoy.

With these two technologies, the use of optical fibers exploded during the 1990s and have since become a vital part of the connected world we live in today. With the growth of data showing no signs of slowing down, it is imperative to improve current systems to meet the demands that the future will hold.

One such area that remains a prominent inconvenience, and thus a possible area for amelioration, for optical fibers is due to nonlinear phenomena. These phenomena occur whenever the polarization density of the medium, the fiber, responds in a nonlinear fashion to the incoming electric field, the incoming signal. As the intensity of the incoming of the signal increases, these nonlinear phenomena start to become more noticeable.

As lasers are used as the source for the signal in fibers, their very high power naturally causes a problem in this regard. This issue is compounded by the fact that the area of the fiber is also made to be very small, due to other factors, which causes the intensity, or power per unit area, of the signal to increase further. Thus, it can be easily understood then that these nonlinear phenomena become evermore present when increasing the launch power into the fiber—a typical preference for communication systems. Although, some of these phenomena can be used in a beneficial way in other applications, in the case here they only cause degrading effects. Therefore any technology which can help mitigate these nonlinear effects would be of great interest.

Such a technology, called multi-subcarrier (MSC) signal processing is the focus of the work presented here. By breaking up one large single-carrier (SC) signal into several smaller signals, or subcarriers, it has been shown that the nonlinear penalties incurred can be reduced. This is because some nonlinear penalties are more prominent at smaller baud rates, whereas other penalties appear more at larger baud rates. Thus by finding the optimal baud rate, or optimal number of subcarriers, for the system to operate at, we are able to reduce the total amount of these penalties. Breaking up a large signal into several smaller ones is not a new concept, as it is already an established method used by orthogonal frequency-division multiplexed (OFDM) systems. However, for MSC systems the subcarriers do not need to be orthogonal to one another and no guard interval is needed between the symbols.

The outline of the thesis is as follows. In Chapter 2, a more in-depth background explanation is given for the key parameters which affect the transmission of the signal along the fiber, as well as the benefits that MSC systems bring in this regard. In Chapter 3, a new algorithm is shown which is needed for removing the

intermediate frequency offset (IFO) which the signal is introduced to. As traditional algorithms used in SC systems for removing this IFO no longer work for MSC systems, this new approach is needed to successfully receive the incoming data without any errors. In Chapter 4 a new approach for generating MSC signals is shown, which makes use of the powerful Fast Fourier Transform (FFT) algorithm. Although MSC systems bring benefits in terms of nonlinear mitigation, they come at the cost of computational efficiency. This FFT technique produces great computational savings as the number of subcarriers increases for these MSC systems, thus allowing them to remain a viable solution to mitigate the nonlinear problem.

Research Publications

1. Ryan Ramdial, Xiaojun Liang, Shiva Kumar, John D. Downie, William A. Wood, "Frequency offset estimation algorithm for a multi-subcarrier coherent fiber optical system," Proc. SPIE 11309, Next-Generation Optical Communication: Components, Sub-Systems, and Systems IX, 113090K (31 January 2020).
2. FFT Based Multi-Subcarrier Processing for Coherent Fiber Optical Systems, submitted to IEEE Photonics, June 2020.

Chapter 2

Background

This section is intended to introduce the design considerations of modern fiber optic systems, the detrimental effects these systems encounter, and current solutions to counteract these effects. Afterwards, it is shown how MSC systems can aid in mitigating some of these effects, namely the nonlinear penalties incurred.

2.1 Cutoff Wavelength

The basic physical structure of a modern fiber is shown in Fig. 2.1. The three components of the fiber are the core, the cladding and the polymer jacket. The transmitted light signal is (ideally) contained solely in the core of the fiber, where it is able to propagate at the furthest possible distance, due to total internal reflection (TIR). TIR occurs due to the small difference between the refractive indices between the cladding and core. This difference in indices creates a critical angle Φ_c at the core-cladding interface. Any ray at the interface with an angle θ greater than this Φ_c will experience TIR. The jacket acts as a physical barrier and protects the fiber from environmental

damage and interference. Instead of thinking of the minimum angle θ that the ray must have at the core-cladding interface, we can use think in terms of the maximum angle launched into the fiber i_{max}, as shown in Fig. 2.2.

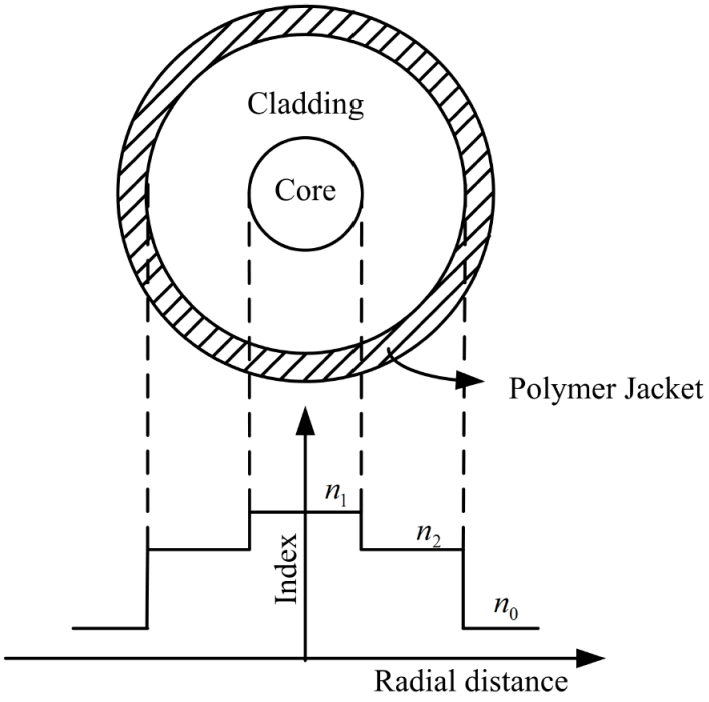

Fig. 2.1: Step-index fiber refractive index profile. [3]

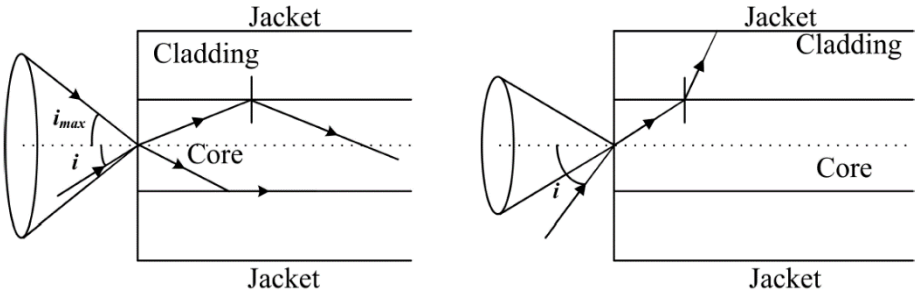

Fig. 2.2: A three-dimensional "cone" of acceptable angles smaller than imax is allowed for TIR. [3]

This allows us to define the term numerical aperture (NA) which can shown to be

$$NA = \sin i_{\max} = (n_1^2 - n_2^2)^{1/2}. \tag{2.1}$$

As there are many possible (though not infinite) angles which can meet this criterion there are many rays, or guided modes, that the optical fiber can support. We call these multi-mode fibers (MMF). However because each mode in a MMF propagates along a different path in the fiber, the light pulse broadens as each mode will take a different amount of time to reach the end. This broadening, known as intermodal dispersion, severely limits the maximum achievable bit-rate, and is a severe limitation for transmitting signals at long distances at high bit-rates. Therefore, for long-haul applications MMF are typically avoided, though the application of few-mode fibers has drawn some interest [4].

To avoid this intermodal dispersion completely we can instead limit the fiber to utilizing only a single mode instead, which is known as single-mode fiber (SMF). To do this we must decrease i_{max} so that only a single ray of a small enough angle can be launched into the fiber. This is done either by minimizing the NA or by decreasing the core radius of the fiber, or both. This leads to the first design constraint, the cutoff wavelength for SMF which is given by

$$\lambda_c = \frac{2\pi a\ NA}{2.4048}, \tag{2.2}$$

where λ_c is the cutoff wavelength, a is the core diameter and NA is the numerical aperture defined in Eq. 2.1). For SMF operation, the operating wavelength must be greater than λ_c. It can easily be seen here that to ensure the operating wavelength meets this criterion, the core radius and the NA should be minimized. This minimization of the core radius is an important point to remember for later on, as in contrast a larger core radius

is desired to minimize the nonlinear penalties. Thus, the need for SMF operation acts as a boundary for how much we can limit the nonlinear interference (NLI) inside the fiber.

2.2 Attenuation, Amplification and ASE Noise

Not unlike other transmission mediums, optical fibers also causes a signal to attenuate while propagating. However, it is the low-loss that optical fibers experience relative to other mediums such as copper or the atmosphere that make them an attractive option. The minimization of the fiber loss is so important that it lays the foundation for the operating frequencies. As introduced in Chapter 1, the search for this loss minimum resulted in three distinct windows to eventually be found, which is shown in Fig. 2.3. The last of these windows—at 1550 nm—is still the standard point of operation for most systems even today. Attenuation in fibers occurs mainly due to two phenomena—Rayleigh scattering and material absorption—though other factors such as bending and splicing losses also play a role.

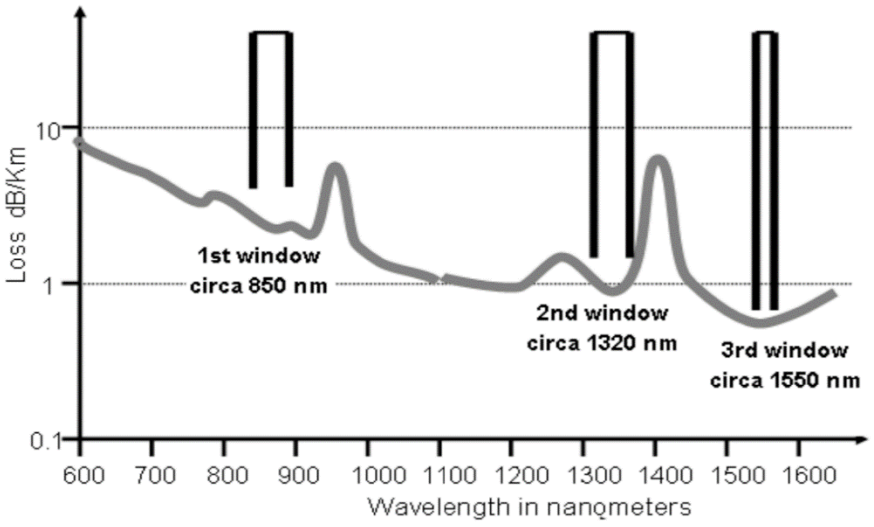

Fig. 2.3: The three operating windows of optical fibers. [5]

Rayleigh scattering is the scattering of light by atoms or molecules of size much smaller than the wavelength of the light. As crystals in the fiber are not isotropic in practice, the irregular spaced atoms cause an

incident ray to be scattered over a range of angles. If any of these angles of scattering are less than the critical Φ_c, that portion of the ray will escape from the core to the cladding, leading to a loss in power. The loss coefficient due to Rayleigh scattering can be shown to be

$$\alpha_R = \frac{1}{\lambda^4}. \tag{2.3}$$

From analyzing Eq. (2.3), it is easy to see that shorter wavelengths will experience more Rayleigh scattering induced losses compared to longer wavelengths. This explains why the loss function in Fig. 2.3 generally trends upwards as the wavelength decreases.

Material absorption comes in two forms: intrinsic and extrinsic. Intrinsic absorption is due to the silica molecule absorbing the incoming photon, which causes a change in the vibrational state of the molecule or a transition of the molecule's electron to a higher energy state. This occurs throughout the wavelength range in Fig 2.3, however it is at longer wavelengths where this absorption becomes more noticeable, hence operations beyond ~1600 nm is rare. Extrinsic absorption is caused by the interaction of light with impurities in silica, though these can mostly be reduced through manufacturing processes. One such important impurity of noticeable importance is due to water vapour. The OH ion of water vapour is bonded to into the glass structure. The vibrational resonances of this combination leads to strong absorption peaks at 880, 950, 1240 and, most visibly, at 1380 nm. Fibers designed to reduced this water peak have been designed later on, resulting in loss profiles such as that shown in Fig. 2.4.

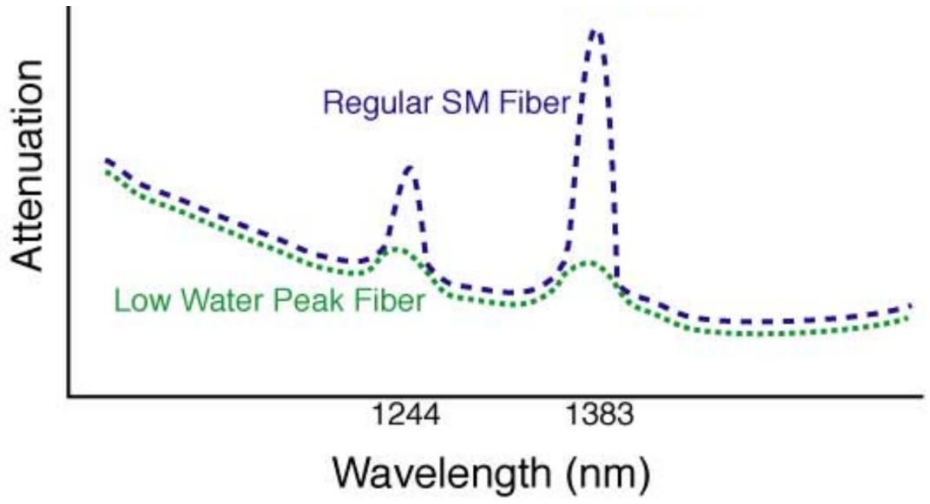

Fig. 2.4: The water peak is reduced when using more advanced fibers, such as G.652D SMF. [6]

To compensate for attenuation over large transmission lengths, the signal must be regenerated once its power diminishes too much. This is known as the span length of the fiber, and is ~100 km for long-haul terrestrial systems when using SMF. EDFAs have become the standard method to amplify the attenuated signals, as mentioned in Chapter 1. For amplification to take place the number of photons being emitted—the stimulated emission rate R_{stim}—from the atomic system must be greater than the number of photons being absorbed into this system, i.e. the absorption rate R_{abs}. When this occurs, we obtain population inversion that can be shown to be

$$\frac{R_{stim}}{R_{abs}} = \frac{N_2}{N_1}, \tag{2.4}$$

where N_1 and N_2 are the atomic densities in the ground state and excited state, respectively. At thermal equilibrium, Boltzmann's law gives this ratio to be

$$\frac{N_2}{N_1} = \exp(-\Delta E / k_B T), \tag{2.5}$$

where ΔE is the energy difference between the excited and ground state, k_B is Boltzmann's constant and T is the absolute temperature. At thermal equilibrium, N_2 is always less than N_1, preventing population inversion to be achieved. Thus to reach a state of population inversion, an external energy source must be used to pump atoms into the excited state. With the aid of such an optical pump, amplification can thus take place via stimulated emission in the fiber at a particular wavelength range. When fibers are doped with the erbium ion Er^{3+}, the gain spectrum—the photons that are formed through stimulated emission—has a peak wavelength of ~1530 nm, as shown in Fig. 2.5. This is very close to the most common operating wavelength of 1550 nm, hence why EDFAs have become the primary means for amplifying signals today. Other mechanisms, such as Raman amplifiers, have benefits as well, however due to costs constraints they are generally only used in conjunction with EDFAs when there is a substantial benefit to be gained.

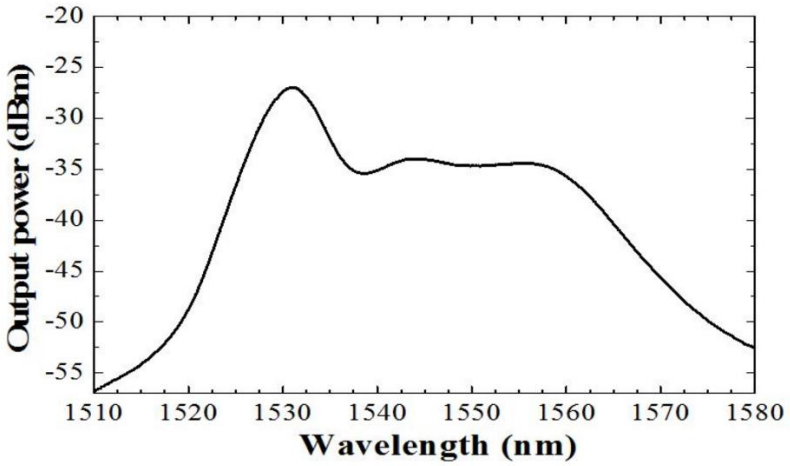

Fig. 2.5: EDFA gain spectrum. [7]

If we represent the loss of the signal in dB as α, then after a length L the output power P_{out} of the signal is related to the input power P_{in} by

$$P_{out} = P_{in} \exp(-\alpha L) . \tag{2.6}$$

If the gain from the amplifier is given by G, then after an ideal amplifier the output power is

$$P_{out} = GP_{in}. \tag{2.7}$$

However, the amplifier adds noise and the total field envelope at the amplifier output is

$$\psi_{tot} = \psi_{out} + n(t) = \sqrt{G}\psi_{in} + n(t). \tag{2.8}$$

The noise term is due to photons which are amplified spontaneously. In stimulated emission, an incident photon in the range of ~1530 nm stimulates the emission of another photon at the same polarization, frequency, phase, and direction. However, an electron can also make a transition between energy states that releases a photon without the need for an incident photon, a process known as spontaneous emission. This released photon does not have the same above-mentioned characteristics as the signal photon. These spontaneously emitted photons are amplified as well in a process known as amplified spontaneous emission (ASE), and acts as noise.

The spontaneous emission factor gives the relations between the population densities in the two energy states as

$$n_{sp} = \frac{N_2}{N_2 - N_1}. \tag{2.9}$$

For an ideal amplifier N_2 is zero—that is full population inversion is achieved. The noise figure is commonly used to characterize the noise added by the amplifier and is given by

$$F_n = \frac{2n_{sp}(G-1)}{G} + \frac{1}{G}. \tag{2.10}$$

Even for an ideal amplifier the lowest achievable noise figure is 3 dB—in other words the noise doubles after passing through the amplifier. In long-haul systems with a chain of amplifiers, the ASE builds up over many amplifiers, degrading the performance of the system and limiting the reach. The power spectral density of the ASE noise for a single polarization can be shown to be

$$\rho_{ASE} = n_{sp}hf_0(G-1), \tag{2.11}$$

where *h* is Planck's constant. After a chain of N amplifiers, the added noise terms add up linearly and the resulting equivalent power spectral density is

$$\rho_{ASE}^{eq} = Nn_{sp}h\bar{f}(G-1). \tag{2.11}$$

Thus, with a large number of amplifiers the amount of noise in the system will eventually be too much to detect the signal,. Although other noise terms, such as thermal noise and shot noise, play a factor as well, for long-haul systems ASE noise by far becomes the dominant term.

One may claim them that to transmit the signal as far and as clean as possible, it is desirable to use the least amount of amplifiers required. To do this the power of the signal should be as large as possible to reduce the number of amplifications needed. However, because of the nonlinear phenomena inside the fiber, any signal power beyond a certain amount will start to have detrimental effects on the system performance. Therefore an optimal signal power exist due to the presence of nonlinearities, which in turn sets the number of amplifiers needed in the system and the amount of noise due to these amplifiers added in too.

2.3 Dispersion

Dispersion in fibers leads to pulse spreading. This spreading causes the pulses to overlap as the transmission distance increases, making the distinct pulses merge into one pulse, and eventually making these separate pulses unrecognizable. This process is shown in Fig. 2.6. This pulse spreading ultimately limits how closely the pulses/data can be spaced together, therefore the ultimate data rate is limited by dispersion.

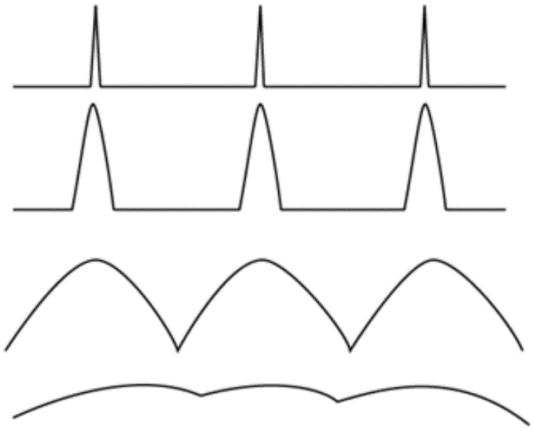

Fig. 2.6: Dispersion causes pulses spreading, making them less distinguishable. [8]

2.3.1 Chromatic Dispersion

The superposition of two monochromatic electromagnetic waves can be written as

$$E = 2\cos(\Delta\omega t - \Delta k z)\cos(\omega_0 t - k_0 z), \tag{2.12}$$

where we assume $\Delta\omega << \omega_0$. This can also be thought of as an optical carrier of frequency ω_0 being modulated by a sinusoid of frequency $\Delta\omega$. The phase and group velocities can then be defined as

$$v_{ph} = \frac{\omega_0}{k_0}, \tag{2.13}$$

$$v_g = \frac{\Delta\omega}{\Delta k}, \tag{2.14}$$

respectively. In a dielectric medium, the velocity of light could vary for different frequencies. Therefore, the phase velocity is a function of frequency, and in turn so to is the phase number

$$k = \frac{\omega}{v_{ph}(\omega)} = k(\omega), \tag{2.15}$$

In general, the group speed can be defined as

$$v_g = \lim_{\Delta k \to 0} \frac{\Delta \omega}{\Delta k} = \frac{d\omega}{dk}. \tag{2.16}$$

Taking the inverse of Eq. (2.16) allows us to define a term we call the inverse group speed, or β_1

$$\beta_1 = \frac{dk}{d\omega}. \tag{2.17}$$

If β_1 changes with frequency for a given medium, we call it a dispersive medium. Using a refractive index that changes with frequency in a given medium, the basic relation for the speed of light in a medium can be shown as

$$v = \frac{c}{n(\omega)}, \tag{2.18}$$

and substituting Eq. (2.18) into Eq. (2.15) yields

$$k(\omega) = \frac{\omega n(\omega)}{c}. \tag{2.19}$$

Subbing in Eq. (2.19) into Eq. (2.17) and differentiating gives

$$\beta_1(\omega) = \frac{n(\omega)}{c} + \frac{\omega}{c}\frac{dn(\omega)}{d\omega}. \tag{2.20}$$

Eq. (2.20) shows that a medium with a variable refractive index will be a dispersive medium, and an optical fiber is such a medium. This is known as material dispersion in optical fibers. The waveguide structure can also introduce dispersion in optical fibers that is known as waveguide dispersion. Different frequency components travel at different speeds in the fiber, leading to pulse spreading. For instance, if two electromagnetic waves are co-propagating with frequencies ω_1 and ω_2, the differential delay ΔT will take to propagate a fixed distance L is

$$\Delta T = |T_1 - T_2| = L|\beta_1(\omega_1) - \beta_2(\omega_2)|. \tag{2.20}$$

The derivative of Eq. (2.17), β_2, called the group velocity dispersion parameter, indicates how much the pulse will spread for a given fiber

$$\beta_2 \equiv \frac{d\beta_1}{d\omega} = \frac{d^2k}{d\omega^2}, \tag{2.21}$$

$$\Delta T = L\left|\beta_2\right|\Delta\omega. \tag{2.22}$$

Finding the derivative of β_1 with respect to wavelength instead, we can define a term called the dispersion parameter D as

$$D = \frac{dk}{d\lambda} = \frac{-2\pi c}{\lambda^2}\beta_2, \tag{2.23}$$

and the differential delay can then be found as

$$\Delta T = DL\Delta\lambda. \tag{2.24}$$

Because the higher frequency components can travel slower or faster than the lower frequency components, β_2 can be either positive or negative. For the former case (higher frequencies being slower), the medium is said to exhibit normal dispersion, and for the latter case it is said to exhibit anomalous dispersion. Optical fiber experience anomalous dispersion around the 1550 nm window. However, the second optical window in Fig. 2.3 (~1320 nm) experiences no dispersion. In fact, this zero-dispersion wavelength was the reason why this second window became successful, along with its relatively low-loss profile too. However, as is shown later, having some dispersion in the fiber is typically desired, as it can reduce some of the nonlinear effects. This dispersion can then be removed at the end of the transmission link using DSP techniques.

2.3.2 Polarization Mode Dispersion

A single mode fiber supports two independent propagation modes [9], which we typically call the x-polarization, with a propagation constant β_x, and y-polarization with propagation constant β_y. For a perfectly circular fiber β_x is equal to β_y; however, fabricating a perfectly circular fiber is extremely difficult. Therefore, due to asymmetry in the fiber and bending, the propagation constants differ, as well as the inverse group speeds for both the x and y-polarizations, β_{1x} and β_{1y}. This makes the signal arrive at the output at different times for the x and y polarizations, leading to pulse broadening. This process is called polarization mode dispersion (PMD). When there is no coupling between the x- and y-polarizations, the differential delay is

$$\Delta T = L\left|\beta_{1x} - \beta_{1y}\right|. \tag{2.25}$$

In practice, coupling is not avoidable. Furthermore, because this coupling is due to random fluctuations in the fiber, modelling the power transfer functions becomes very difficult. However, as these functions change over a time scale much longer than the symbol period, we can instead estimate the transfer function and compensate for it using DSP.

2.4 Multiplexing Techniques

An upper limit exist for symbol rates in single-channel transmission, due to electronic speed limitations of transmitter and receiver circuits. Therefore, to achieve data rates that meet modern demands, multiplexing techniques must be used.

2.4.1 Polarization-Division Multiplexing

Because a single-mode fiber supports two polarization modes [9], information can be transmitted using both of these polarizations. This is known as polarization-division multiplexing (PDM), and is universally used in communications systems today, as the data rate is instantly doubled. A polarization beam splitter is used to split the x- and y- polarization components of the laser source. An example of how PDM is achieved at the transmitter is shown in Fig. 2.7.

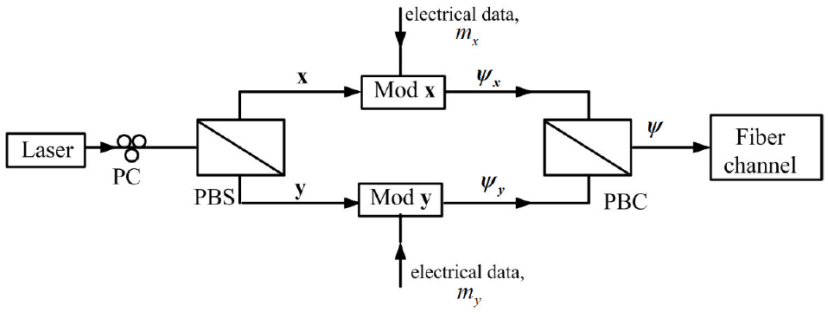

Fig. 2.7: PDM setup at transmitter. [9]

2.4.2 Wavelength-Division Multiplexing

As seen in Fig. 2.5, the amplification range of EDFA extends from 1530-1565 nm, or about 4.3 THz. A single channel makes use of only a fraction of this bandwidth. Therefore, multiplexing several channels together allows the data rate to increase substantially, while still only using a single fiber. For N carriers each of data rate B, the total data rate is N·B. Therefore, to maximize the total data rate the number of channels that can fit inside the 4.3 THz spectrum should be maximized. However, the channel spacing Δf must be larger than or equal to the signal bandwidth otherwise the channels will overlap. Too large of a channel spacing though, and the bandwidth of the fiber is partially wasted. The spectral efficiency η is a metric which gives an idea of how well the fiber's bandwidth is being used and is defined as

$$\eta = \frac{B}{\Delta f}. \tag{2.25}$$

With a fixed channel spacing, the only way to increase the spectral efficiency is to increase the data rate. This can be done by using PDM systems, as well as using higher order modulation formats. However, the transmission distance for signals with higher modulation formats are limited due to nonlinear effects. Therefore a tradeoff between spectral efficiency and reach.

2.5 Nonlinear Effects

2.5.1 Kerr Effect

An optical fiber is a nonlinear system because the refractive index of the fiber varies with the intensity of the signal propagating through the fiber. In the linear case the relative permittivity ε_r is related to the first-order susceptibility $\chi^{(1)}$ by

$$\varepsilon_r = 1 + \chi^{(1)}, \tag{2.26}$$

which can be shown is related to the refractive index as

$$n^2 = 1 + \chi^{(1)} = 1 + \frac{Nq_e^2}{m\varepsilon_0(\omega_0^2 - \omega^2)}. \tag{2.27}$$

The refractive index is dependent on the frequency and leads to chromatic dispersion as seen already seen. Eq. (2.27) assumes the polarization is related to the electric field intensity linearly as

$$\mathbf{P} = \varepsilon_0 \chi^{(1)} \mathbf{E}. \tag{2.28}$$

Eq. (2.28) hold true when the incident signal is weak, however as the power increases this no longer holds true and instead this relationship is a function of the electric field intensity in terms of increasing powers

$$\mathbf{P} = \varepsilon_0 \chi^{(1)} \cdot \mathbf{E} + \varepsilon_0 \chi^{(2)} \cdot \mathbf{EE} + \varepsilon_0 \chi^{(3)} \cdot \mathbf{EEE} + \ldots \quad . \tag{2.29}$$

The second-order susceptibility, $\chi^{(2)}$, is not a factor for optical fibers as silica is a symmetric molecule. The third harmonic generation $\chi^{(3)}$ does factor in, and is responsible for third harmonic generation and the Kerr effect.

For a centrally symmetric dielectric material with an electromagnetic field only containing E_x and H_y components, Eq. (2.29) can be simplified to obtain

$$P_x = \varepsilon_0 \chi_{xx}^{(1)} \cdot E_x + \varepsilon_0 \chi_{xxxx}^{(3)} \cdot E_x^3 . \tag{2.30}$$

This in turn modifies Eq. (2.27) to be

$$\begin{aligned} n^2 &= 1 + \chi_{eff} = 1 + \chi_{xx}^{(1)} + \frac{3|E_0|^2}{4} \chi_{xxxx}^{(3)} \\ &= n_0^2 + \frac{3|E_0|^2}{4} \chi_{xxxx}^{(3)} \end{aligned} , \tag{2.31}$$

where n_0 is taken to be the linear refractive index. As the nonlinear part of the refractive index is typically much smaller than the linear apart, Eq. (2.31) can be approximated as

$$n \cong n_0 + n_2 |E_0|^2 . \tag{2.32}$$

n_2 is known as the Kerr coefficient and is found from Eq. (2.31) and Eq. (2.32)

$$n_2 = \frac{3\chi_{xxxx}^{(3)}}{8 n_0} . \tag{2.33}$$

The refractive index is directly proportional to the optical intensity in Eq. (2.32), which is known as the Kerr effect, and is the source of nonlinear phenomena in optical fibers.

With dispersion and the Kerr effect taken into account, an optical signal propagating through the fiber can be described by the nonlinear Schrödinger equation (NLSE)

$$i\frac{\partial q}{\partial Z}-\frac{\beta_2}{2}\frac{\partial^2 q}{\partial T^2}+\gamma|q|^2 q=-i\frac{\alpha q}{2}, \tag{2.34}$$

where γ is the nonlinear coefficient and can be found to be

$$\gamma=\frac{n_2\omega_0}{cA_{eff}}. \tag{2.35}$$

In Eq. (2.35), it can be seen that by increasing the effective area A_{eff} of the fiber the nonlinear phenomena will decrease. However, as mentioned in Section 2.1, the fiber has a maximum dimensional area if it is to operate as a SMF. The Kerr effect produces different kinds of nonlinear effects such as self-phase modulation (SPM), cross-phase modulation (XPM), and four-wave mixing (FWM).

2.5.2 Self-Phase Modulation

Ignoring the β_2 term in the NLSE (Eq. (2.34)), and separating the amplitude and phase terms as

$$q=Ae^{i\theta}, \tag{2.36}$$

the NLSE becomes

$$i\left[\frac{\partial A}{\partial Z}+i\frac{\partial\theta}{\partial Z}A\right]=-[\gamma A^2+i\frac{\alpha}{2}]A. \tag{2.37}$$

Solving for this equation yields the result

$$q(T,L)=q(T,0)e^{-\alpha L/2+i\gamma|q(T,0)|^2 L_{eff}}, \tag{2.38}$$

where L_{eff} is the effective length of the fiber and is defined as

$$L_{eff}=\frac{1-e^{-\alpha L}}{\alpha}. \tag{2.39}$$

The phenomenon in Eq. (2.38) of the phase of the signal being modulated by it's own power distribution is known as SPM. This effect causes some frequency components in an optical pulse to be blue-shifted, while other components to be red-shifted. The total effect creates new frequency components and thus a larger spectral width. Because of dispersion in the fiber, this increase in spectral width causes the pulse to spread further in the time-domain as well, and ultimately affects the achievable data rate.

2.5.3 Cross-Phase Modulation

The benefits of WDM systems have been mentioned in Section 2.4, however there exits drawbacks to these systems as well. For N channels transmitted the total field envelope Ψ can be described as

$$\Psi = \sum_{n=-N/2}^{N/2-1} q_n(t,z) e^{-i(\omega_n t - \beta_n z)} . \tag{2.40}$$

Eq. (2.40) can be written instead relative to the centre frequency ω_0 as

$$\Psi = q e^{-i(\omega_0 t - \beta_0 z)}, \tag{2.41}$$

$$q = \sum_{n=-N/2}^{N/2-1} q_n(t,z) e^{-i(\Omega_n t - \delta_n z)}, \tag{2.42}$$

where the relative centre frequency Ω_n is

$$\Omega_n \equiv \omega_n - \omega_0 . \tag{2.43}$$

Ignoring the other nonlinear effects for the time being, the NLSE is then modified to be

$$i\left(\frac{\partial q_n}{\partial Z} + d_n \frac{\partial q_n}{\partial T}\right) - \frac{\beta_2}{2}\frac{\partial^2 q_n}{\partial T^2} + \gamma\left(|q_n|^2 q_n + 2\sum_{k=-N/2}^{N/2-1} |q_k|^2 q_n\right) = -i\frac{\alpha}{2} q_n , \tag{2.44}$$

where d_n is known as the walkoff parameter and is calculated as

$$d_n = \beta_2 \Omega_n . \tag{2.45}$$

Due to the Kerr effect, co-propagating pulses with different wavelengths induce a nonlinear phase shift on each other. This phase shift is time-dependent, ths the instantaneous frequency across a pulse in a channel is modified and new frequency components are generated. In a dispersive fiber this frequency shift is translated into a timing shift since different frequency components propagate at different speeds [3]. Therefore, the co-propagating pulses arrive at different times and we say one pulse "walked-off" the other.

The frequency components generated due to XPM travel at different speeds and arrive at different times at the fiber output, leading to a timing jitter and amplitude modulation. This results in less ideal decision making at the receiver, thereby degrading the system. However, with dispersion, XPM becomes less prominent over the length of the fiber, as the co-propagating channels walk-off from each other and have less of an influence on one another. Therefore, even with the mentioned drawbacks of dispersion in Section 2.3, it is important for the fiber to have some of dispersion in it to counteract XPM.

2.5.4 Four-Wave Mixing

Using Eq. (2.41) and Eq. (2.42) while ignoring the other nonlinear effects, the NLSE when only considering FWM is modified to be

$$\frac{\partial q_n}{\partial Z} + \frac{\alpha}{2} q_n = i\gamma \sum_{j=-N/2}^{N/2-1} \sum_{k=-N/2}^{N/2-1} \sum_{l=-N/2}^{N/2-1} q_j q_k q_l^* e^{i\Delta\beta_{jkl\text{-}n} Z} . \tag{2.46}$$

Here, three waves of different frequencies leads to the generation of a fourth wave. Either the frequency of this new wave can be different from the initial three waves, or it can be the same as one of them. When the latter case occurs, we have what we refer to as FWM. This FWM field acts as

noise on the channel it is afflicting, thus degrading the overall performance. The greater the power of the initial fields, the more noise will be present. As with XPM, having some dispersion in the fiber can reduce the FWM effects as the channels are no longer integer multiples of one another and thus the fourth field being generated no longer falls on one of the three original fields.

2.5.5 Other Nonlinear Effects

SPM, XPM, and FWM are all nonlinear phenomena due to the Kerr effect inside an optical fiber. However, there are other effects, namely stimulated Brillouin scattering (SBS) and stimulated Raman scattering (SRS), which can also occur. For these effects to be noticeable though, the signal power must be greater than a certain threshold. The other nonlinear effects (SPM, XPM, FWM) also increase with increasing powers; however, a lower power level is needed to observe the detrimental effects they cause. Therefore, SBS and SRS are typically not of much concern for most long-haul communications systems, unless the SRS effect is used in a beneficial manner for producing Raman amplification. An overview of all linear and nonlinear effects is shown in Fig. 2.8.

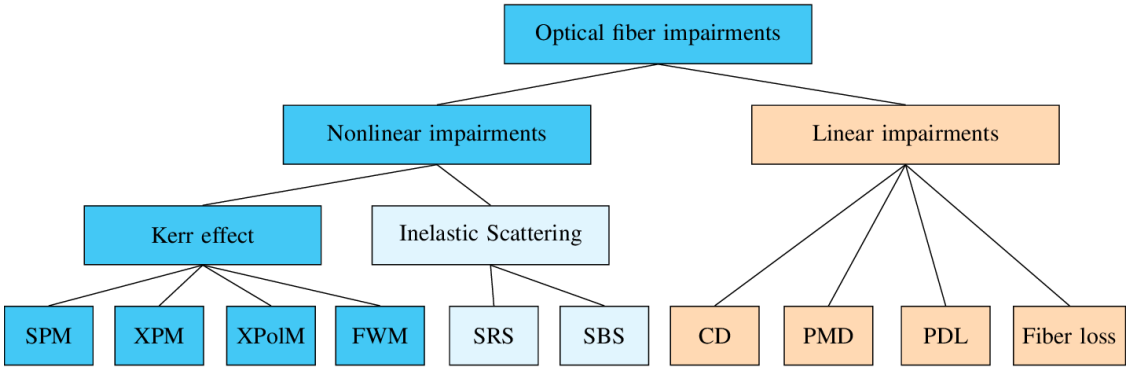

Fig. 2.8: Overview of fiber impairments. [10]

2.6 Nonlinear Effects on Channel Capacity

[11] Provides a theoretical model of how much data can be sent along a transmission link. The equation states that the total channel capacity C is related to the bandwidth B and the signal-to-noise ratio (SNR) by

$$C = B \cdot \log_2(1 + SNR). \tag{2.47}$$

This states that there are two options to increase the total data rate: either increase the bandwidth and/or increase the SNR of the signal. For optical fibers, a bandwidth limitation exists due to the need for operation within the EDFA gain spectrum for transmitting the signal at a low-loss level, though this is slightly changing with L-band transmission being in use too [12]. Nevertheless, increasing the SNR is the de facto practice.

However, to increase the SNR either the signal's power must be increased or the noise level must be decreased. Amplification is relatively expensive in practical systems, and therefore finding the optimum number of amplifiers while still reducing the noise level is typically done. This in hand means the noise level is fixed to the amplifier spacing, leaving increasing the signal power as the sole option.

However, as seen in Section 2.5, increasing the signal's power makes detrimental nonlinear effects to become more prominent. In fact they become so prominent that after a certain point, the channel capacity in Eq. (2.47) starts to decrease with increasing power level, as shown in Fig. 2.9 [13].

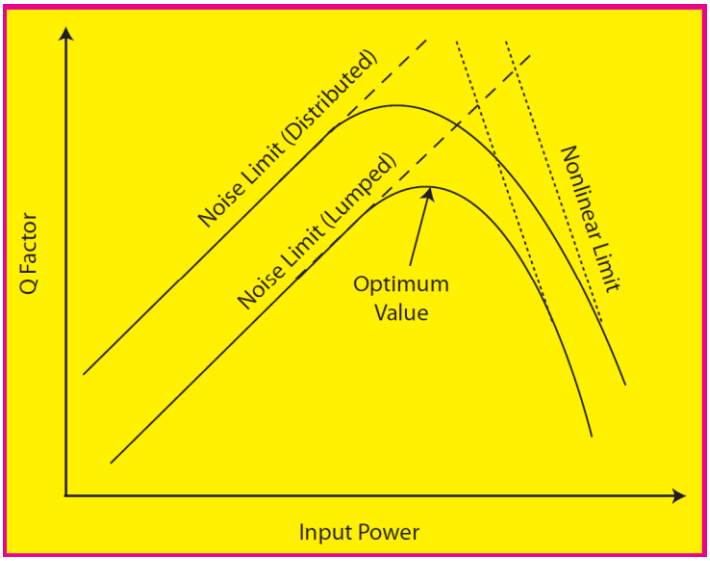

Fig. 2.9: An optimum point exists for input power due to nonlinear effects. [14]

These nonlinear effects therefore act as a great limitation to achieving data rates required for the ever-increasing demand. Thus, reducing these effects has drawn much attention. Methods such as digital back-propagation (DBP) exists, which work decently well, however DBP does not successfully remove all of the nonlinear effects. A relatively new method, called multi-subcarriers (MSC) processing is a promising technique as it has also shown to be able to decrease these nonlinear effects, which can work in conjunction with current methods such as DBP. This thesis relates to advances in current MSC processing techniques, and thus some cursory knowledge is required as to why MSC techniques aid in reducing nonlinear effects.

2.7 Multi-Subcarrier Processing

Although DBP is effective in mitigating some NLI penalties, it can only remove penalties for the channel it is operating on. DBP cannot operate on the entire WDM system due to being very computationally complex to do so and, more importantly, different channels in WDM system are added/dropped at any span end using

reconfigurable optical add-drop multiplexers (ROADM), making it impractical to know which channels were effecting the channel we are interested in. Thus the NLI impact other channels have is typically treated as noise, and more specifically was considered additive-white Gaussian noise (AWGN), which is referred to as a Gaussian-noise (GN) model. While satisfactory to use this model in some scenarios, it is inaccurate in other scenarios. The main inconsistency is that the NLI noise interfering from other channels is modulation-format dependent, something that the GN model does not take into account, as it ignores the statistical dependence between different frequency components of the interfering channels. In [15] it is shown that the variance of the NLI noise when taking into account statistical dependencies is given by

$$\sigma_{NLI}^2 = P^3\chi_1 + P^3\chi_2\left(\frac{\langle|b|^4\rangle}{\langle|b|^2\rangle^2} - 2\right), \tag{2.48}$$

where P is the average power, b is the data symbol in the interfering channel and χ_1 and χ_2 are given in [15]. The second term in Eq. (2.48) is the missing term from the GN model. This noise term is related to the kurtosis of the random variable and, as it is of the fourth-order, is considered a fourth-order noise (FON) term. When taking into account the FON term a new model is formed which is referred to as enhanced Gaussian-noise (EGN) model [17].

This presence of this FON term implied modulation formation dependence. For different modulation formats, examples this noise term are

$$\sigma_{NLI,QPSK}^2 = P^3\left(\chi_1 - \chi_2\right), \tag{2.49}$$

$$\sigma_{NLI,QAM16}^2 = P^3\left(\chi_1 - 0.68\chi_2\right), \tag{2.50}$$

$$\sigma_{NLI,Gaussian}^2 = P^3\chi_1. \tag{2.51}$$

Here we can see that the variance of the NLI noise is reduced for any non-Gaussian modulation format. This can also be thought of qualitatively since lower modulation formats are less Gaussian-shaped, and thus would differ the most when the FON term is considered.

In [16] it was shown that for on-off keying systems, carrying data at any given rate, would be affected by the channel granularity in a nonlinear channel. This would mean that transmitting information on a high baud-rate carrier would be sub-optimal for system performance. It was proposed then that if there was a benefit for direct-detection systems, then it could potentially be one too for coherent-based systems. In [18] this premise was shown to be true, and the benefits of subcarrier bring are shown in Fig. 2.10. [19-21] give further prove to these results. The explanation for this been described in detail in [18], though in short it is explained by considering the spectra of intensity-fluctuations together with the XPM efficiency. Another way to explain this since not all nonlinear phenomena originate from the same source, different nonlinearities will be greater at certain symbol rates and smaller at other ones. Finding the point where the total cumulative nonlinearities is smallest gives the optimal symbol rate as shown in Fig. 2.11.

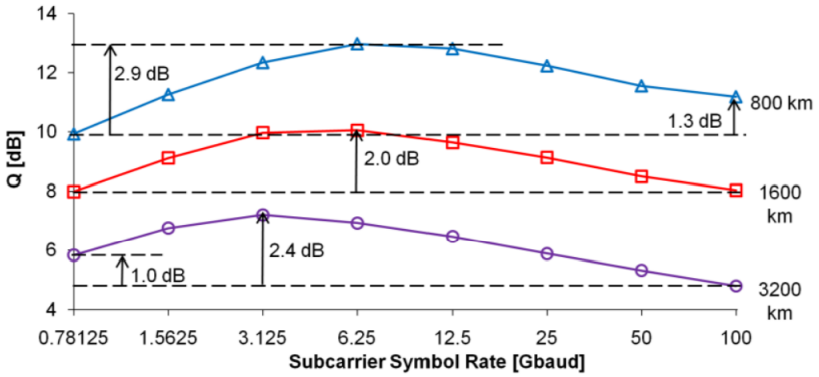

Fig. 2.10: The system improvement from using subcarriers is shown in terms of Q-value here. [18]

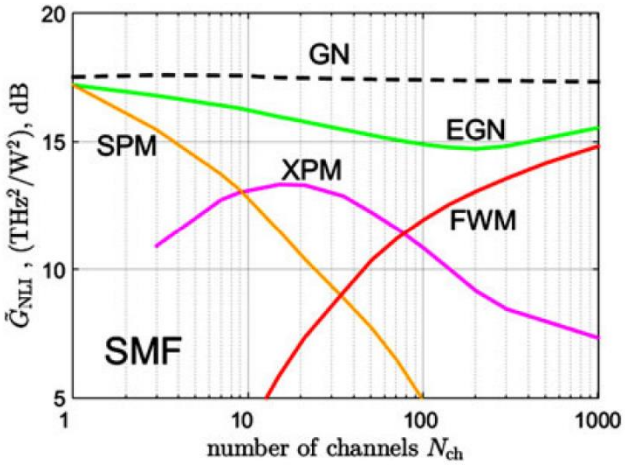

Fig. 2.11: Optimal symbol rate is point at which total nonlinearity penalties is smallest (lowest value of green curve). [22]

Although proven experimentally, the GN model was still being used which did not allow the experiments to coincide with simulations. It was not until [23] where it was discovered that the EGN model was needed for simulations to coincide with experiments. The similarities between simulations and experiments could now easily be seen, as shown in Fig. 2.12.

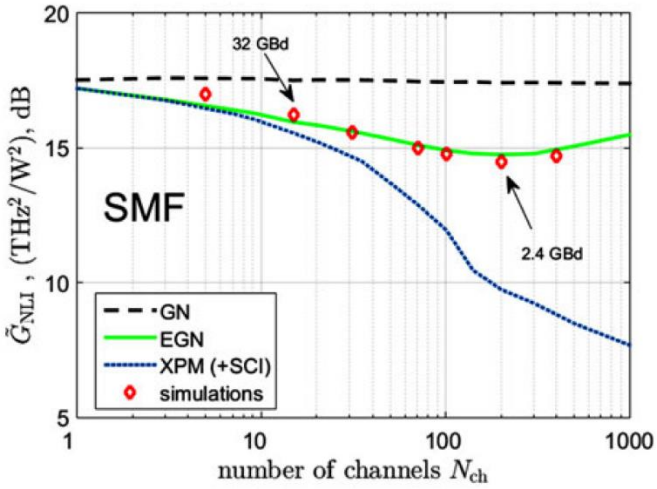

Fig. 2.12: Only the EGN model can accurately show benefits of MSC systems. [22]

[23] also provided a closed-form solution for giving the optimal symbol rate

$$R_{opt} = \sqrt{2/(\pi|\beta_2|L_{span}N_{span}}\ . \tag{2.52}$$

As previously shown in Eqs. (2.49-2.51), the NLI noise is smaller for lower modulation formats as they are less Gaussian-like in nature. However, the NLI term describer here does not make a distinction between nonlinear phase noise (NLPN) and the more commonly thought of amplitude noise. In theory, as a significant portion of the NLI noise can be considered NLPN, it could be eliminated using more sophisticated DSP, however this DSP setup was not used in any experiments we did, and thus higher-modulation formats perform worse than lower ones. Furthermore, distributed (Raman) amplification increases the amount of nonlinear mitigation compared to lumped amplification systems, especially as the span of the system increases as shown in Fig. 2.13. However as our simulations do not currently possess Raman amplification, these benefits could not be realized.

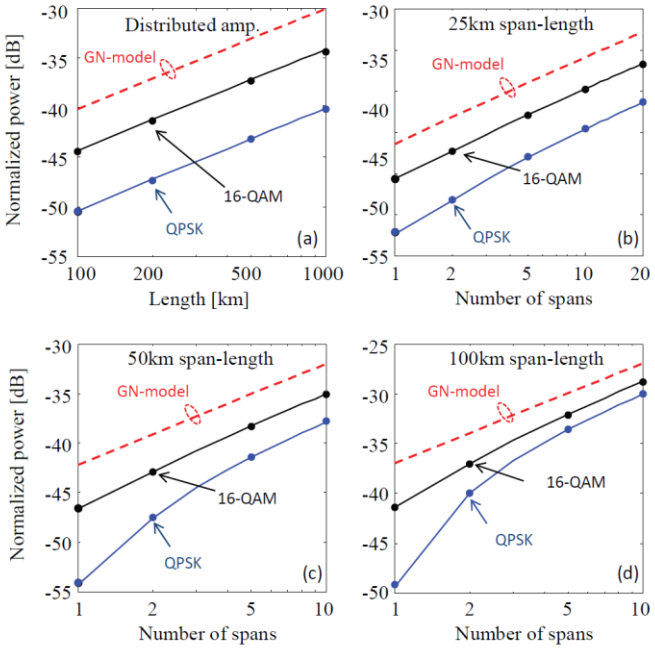

Fig. 2.13: The greatest benefits of MSC systems is seen when using distributed amplification. [24]

Finally, although current methods such as DBP exist to reduce NLI penalties, MSC systems could be used in conjunction to decrease these penalties further. As shown in [25], using DBP and MSC together gives a 13% gain in system performance. This gain is greater than if either DBP or MSC were used independently (9% gain each), although the sum of using the two together is less than the sum of individual use, indicating there is some crossover in mitigation of NLI.

With ever-increasing data rates, the interest of channels with greater throughput have been of growing interest [26], which in turn need requires the need for MSC systems more than ever to operate at an optimal point. MSC systems however face some different challenges from a DSP perspective compared to SC systems. Improvements of some of these DSP problems is the focus of the next two chapters.

Chapter 3

Frequency Offset Estimation Algorithm

This chapter introduces a novel algorithm that can be used to remove the intermediate frequency offset (IFO) which are ever-present in coherent-based communication systems. This new technique is needed as traditional algorithms that work for SC systems no longer work for MSC ones. A brief overview of the origin of IFO is given before the introduction of the new algorithm is shown. As this method works by moving from the "best guess" to the "next best guess", it is considered an estimation algorithm.

3.1 Origins of Intermediate Frequency Offset

With the ever-increasing need to increase the spectral efficiency of communication systems, higher-level modulation formats have become a standard practice for most fiber-optic systems (sub-oceanic

being the one exception due to additional constraints). If B_s is the number of symbols per second transmitted, it is equivalent to transmitting B bits per second as follows

$$B = B_s \log_2 M \,, \tag{3.1}$$

where M is the modulation level. However, to actually detect the signal at the transmitter, coherent detection receivers are needed, as they are able to detect both amplitude and phase of the incoming signal. In contrast, direct detection receivers, although simpler to build, are only able to identify the amplitude of the signal, making them ineffective if higher-order modulation formats are to be used. The entirety of the coherent receiver can also be implemented in the digital domain these days using modern-day DSP, making it a more attractive option compared to systems of the past that used phase-locked loops [27].

After transmission through the fiber, the received signal can be represented as

$$q_r(t) = A_r s(t) \exp[-i(\omega_c t + \phi_c)], \tag{3.2}$$

where s(t) is the complex field envelope, ω_c is the frequency of the optical carrier, and A_r^2 is the peak received power. The local oscillator's (LO)—needed for coherent detection to take place—output signal can be similarly represented as

$$q_{LO}(t) = A_{LO} s(t) \exp[-i(\omega_{LO} t + \phi_{LO})]\,. \tag{3.3}$$

These two signals are then combined using a 3-dB coupler and pass through a photodetector. After noticing the LO power is much larger than the signal power and removing a D.C. component, the photocurrent is

$$I_d(t) = R A_r A_{LO} \,\mathrm{Re}\left\{ s(t) \exp[-i(\omega_{IF} t + \phi_c - \phi_{LO})] \right\}, \tag{3.4}$$

where R is the responsitivity and ω_{IF} is the IFO term. This term is random within a given range and therefore cannot be removed using a priori knowledge. However, it must be removed before further DSP at the receiver is done, as this term causes the absolute value of the phase to increase with time, leading to erroneous phase decisions and rendering coherent detection ineffective. An example of this phase function without and without the removal of the IFO is shown in Fig. 3.1.

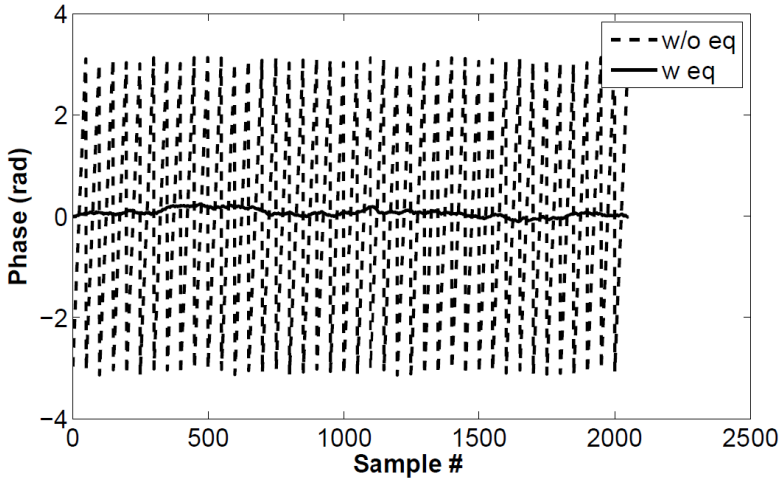

Fig. 3.1: Phase function of signal after mixing with LO with and without equalization of IFO. [3]

Various techniques exists that can successfully remove the IFO, such as the phase increment algorithm [28], Tratter IF estimation algorithm, and Kay IF estimation algorithm [29]. However, these methods were created for SC systems in mind. For MSC systems, as the subcarriers are multiplexed together, it is impossible to know what part of the data belongs to which subcarrier, making these algorithms ineffective. Also, the subcarreris cannot be demultiplexed first and then have the algorithms applied to them, as the IFO would be removed after the demultiplexing stage and be lost forever. Therefore, a new method for estimating the IFO for MSC systems is needed, and such a method is laid out in this chapter. This method is the same as that in [30].

3.2 Algorithm Design

From Eq. (3.4) the signal which we are interested in, s(t), is multiplied by the complex exponential term which contains the IFO value (the phase components can be ignored here). Using the Fourier transform property

$$s(t)e^{i\omega_0 t} \rightleftarrows S(\omega-\omega_0), \tag{3.5}$$

it can be concluded that this IFO term will lead to a shift in the frequency spectrum between the transmitted and received signals. Therefore, if this shift can be detected from than the IFO term can be effectively removed.

One way to detect this shift it find the edges for both the transmitted and received signals' spectrums. The corresponding difference would then correspond to the IFO term wanted. There are two sides of which can be used for detection, positive and negative frequency edges; however, we chose to focus only on using the positive values, though negative values could also be used. These edges are shown in the red box in Fig. 3.2. The bandwidth of this signal is 60 GHz, however the difference between the edges are typically in the order of less than 1 GHz.

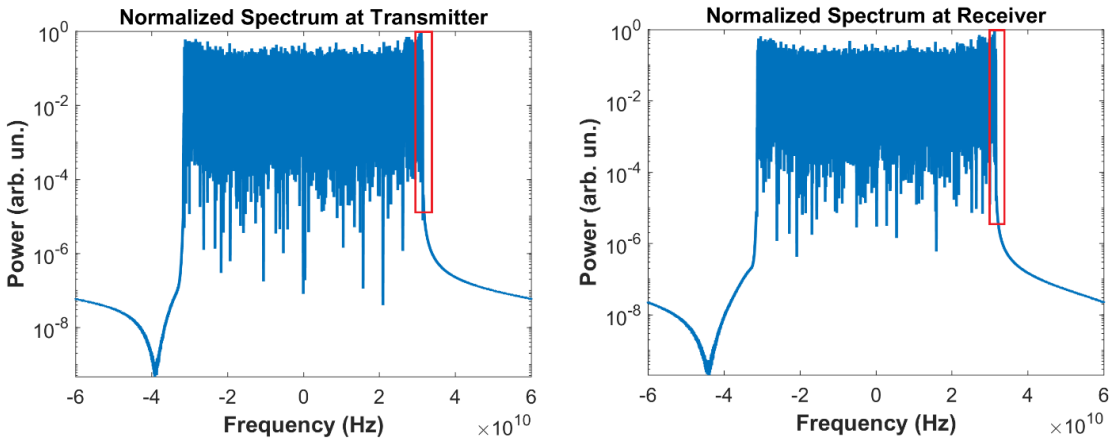

Fig. 3.2: Difference between edges the transmitted and received signals' spectrum should give IFO.

This method of course depends on the ability to accurately detect the edges. To do so, an idea similar to some basic image processing algorithms is utilized. As can be seen in Fig. 3.3, the maxima of the first derivative of the intensity function of the image should indicate where the edges in that image are. Similarly, detecting the location in the spectra where the gradient has the largest magnitude should indicate where the edge is, since the edges of the spectra drop off the most there.

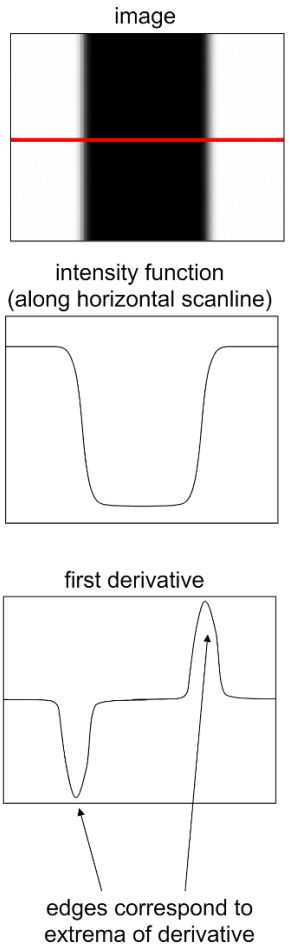

Fig. 3.3: First derivate of image can be used to detect edges.

Although in principle only the true edge should be sharp, in practice, due to the noise and distortions introduced by the system, there are many sharp edges. By first locating the spectral edges of the transmitted and received signals, we are able to narrow down the search area of the IF offset. This range of frequencies is sorted into an array in order of descending power, as it was observed empirically that the correct edges typically lie at or near a local maximum of the spectrum's power, with the largest peaks more likely to produce the correct estimate. Using this estimated IF offset, we can then demultiplex each subcarrier of the received data. We find the cross-correlation (XC) between the received data and the transmitted data using the training sequence for each subcarrier. The XC values for all the subcarriers will be close in value if the correct IF offset was chosen, therefore the XC values also act as a verification. If the estimated IF does not pass this verification, we use a loop to move on to the next element in the array and continue this same process until the correct frequency is detected.

To test our algorithm, experiments have been done using 12 subcarriers at 5 GBaud per subcarrier dual polarized QPSK data (total data rate per channel = 240 Gb/s), 8 channel WDM, and a transmission over a link length of 6000 km with 100-km long spans of Corning® TXF® optical fibers. The new algorithm is used successfully over this system and the mean Q-factors at the optimal launch power are found to be 9.4 dB and 10.1 dB with and without DBP, respectively.

3.3 Experimental Setup

The experimental setup is shown in Fig. 3.4. At the transmitter, 12 subcarriers operating at 5 GBaud are multiplexed together to obtain a 60 Gbaud (per polarization) signal. The modulation format on each subcarrier is quadrature phase-shift keying (QPSK). Root-raised cosine (RRC) pulses

with a roll-off factor of 0.05 produce a total signal bandwidth of 63 GHz. The channel of interest is modulated using an optical IQ transmitter (60 GBaud Multisubcarrier Tx in Fig. 3.4), while all other wavelength division multiplexed (WDM) channels are modulated using a different optical modulator (λ_1 to λ_n in Fig. 3.4). The WDM signal has 8 channels spaced by 75 GHz in frequency. The acoustic-optical modulators (AOMs) are used to control the recirculating loop that consists of six spans of TXF fibers, Erbium doped fiber amplifiers (EDFAs) and a gain equalization filter (GEF).

The fiber spans have 100 km average length, 17.58 dB average span loss including splices and connector losses, 21 ps/(nm.km) chromatic dispersion and 125 μm2 effective area. At the receiver, signals at the channel of interest are received by a 90 degree optical hybrid followed by a real-time oscilloscope with 65 GHz bandwidth and 160 Gsa/s sampling frequency. Then, the off-line DSP begins by implementing: front-end correction and resampling. Afterwards, the signal is compensated either from DBP or from chromatic dispersion compensation (CDC)—DBP compensates for both intra-channel nonlinearities and dispersion impairments, whereas CDC compensates for chromatic dispersion only. The DBP is realized using the well-known split-step Fourier technique.

Next, the signal passes through the frequency offset compensation block using the edge detection algorithm, which is the main purpose of this paper and is discussed in detail in section 3. The subcarriers are demultiplexed using a matched filter (RRC filter) and each subcarrier passes through Constant Modulus Algorithm (CMA) and phase-noise compensation blocks. At last, the bit error rate (BER) is calculated by direct error counting.

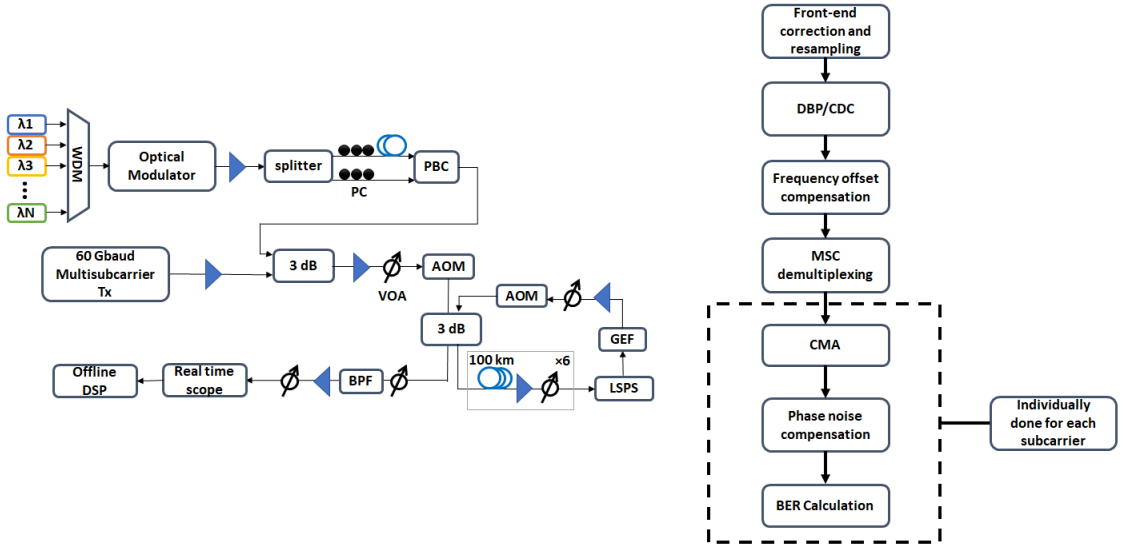

Fig. 3.4: Experimental setup and block diagram of receiver side DSP.

3.4 Edge Detection Algorithm

3.4.1 Detection of spectral edges

Although in theory the transmitted edge should already be known ((Baud Rate x (1 + Roll-Off Factor))/2), for the experimental results this does not always hold true. Therefore, the calculation of the transmitted spectral edge can be done before transmission and be sent to the receiver. We first take the Fourier transform of the transmitted data in each polarization, take the absolute square and add them together to obtain the total power spectral density. From knowledge of the bandwidth of the channel under test, we can take a window of the transmission (TX) spectrum of where the spectral edge should occur. We focus on the positive frequencies for this spectrum only, although it is possible to obtain the same results using the negative half of the spectrum. For the 60 GBaud system we used, this would correspond to taking a window around the 30 GHz point. With a frequency step size of approximately 1.22 MHz used in our experiment, a window of 4000 samples

was taken. This gives a window range between 27.6 GHz and 32.4 GHz. An example of this window is shown in Figure 3.5. Although this windowing is not necessary, it makes the algorithm faster by making a rational guess of where the edge will lie, thus ignoring irrelevant frequencies. This also makes it less prone to errors which may be present elsewhere in the spectrum.

With the possible frequencies narrowed in, we then further divide this window into blocks of 50, sum over each of these smaller blocks, and then divide by 50 to get the average power over this range. The purpose of this averaging is to reduce the effects of noise. A block size of 50 was chosen as it produced the best results compared to other block sizes of 25, 40 and 100. An array of the derivatives from these blocks was formed and the block at which the (negative) difference is the largest corresponds to the edge of the spectrum as that is where the power of the spectrum drops off the most. The summing into blocks of 50 becomes evident here, as it essentially acts as a low-pass filter to remove the sharp transitions that would lead to large, incorrect differentials. This new array was then sorted in ascending order. We used two criteria to ensure that the chosen block was the correct choice.

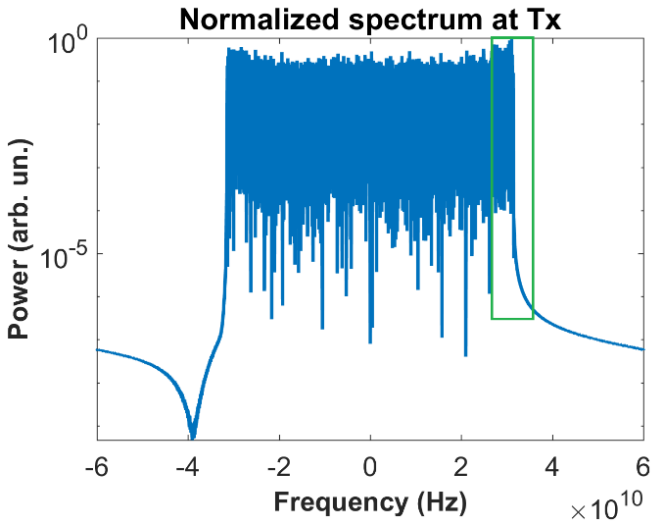

Fig. 3.5: Approximate window taken of frequencies used in narrowing down search.

The first criterion was used to ensure we did not make an underestimation (2 or more blocks away from correct choice). We did this by looking at the "decay rate" of some blocks following the one that was chosen. As the correct block lies at the edge of the spectrum, after a small transition the following blocks should have a noticeably smaller power level compared with the correct block. Therefore, if there were a large underestimation of the desired block, the blocks following it would not have their power levels decreased substantially. We can then test the next block in the differential array using a loop, and continue to test this criterion until the correct block is chosen. For the transitional period, we used a spacing of 3 blocks (150 samples). Therefore, we compare the chosen block with the fourth, fifth, and sixth blocks after it, and made sure the power ratios between the chosen block and these test blocks was greater than a certain value (a ratio of 1.5 was used in our tests). Comparing with 3 blocks instead of just 1 makes the decision less prone to any errors arising from possible anomalies in the spectrum. An incorrect chosen block is shown on the left image of Figure 3.—the detected (red block) was chosen, however as can be seen the blocks after the transition period do not decrease by a substantial amount in power level.

The second criterion was used for possible overestimations that may occur. Again, by looking at the power level at the chosen block it should be in a similar range to the power levels of the preceding blocks. Therefore, if an overestimation were to occur, the ratio between the chosen block and the blocks prior to the edge would be a small value. To obtain a reference of what the power should be, we took the average over the first 10 blocks in the window, as it is extremely unlikely that the actual correct block would lie there. We could then test the chosen block's power level with the average of these 10 blocks, and move on to the next estimated block in the array if it did not pass this ratio test using the same loop as before. A desired ratio of 0.9 was chosen in our experiment. An example of an incorrect detection from overestimation is shown in the middle image of Fig. 3.6.

In the top left of Fig. 3.6 an underestimation (red window) of the correct block (green) is shown. As the blocks (yellow) following the red one do not "decay" in power past the required threshold, we conclude that the incorrect block was chosen. In the top right there is an overestimation: blocks after the red do decay, but comparing the power level of the red block with the average power level of the first 10 blocks (brown window) indicates that this too is the wrong block (too weak in power level). The bottom has the correct block detected as there is a decay and has appropriate power level.

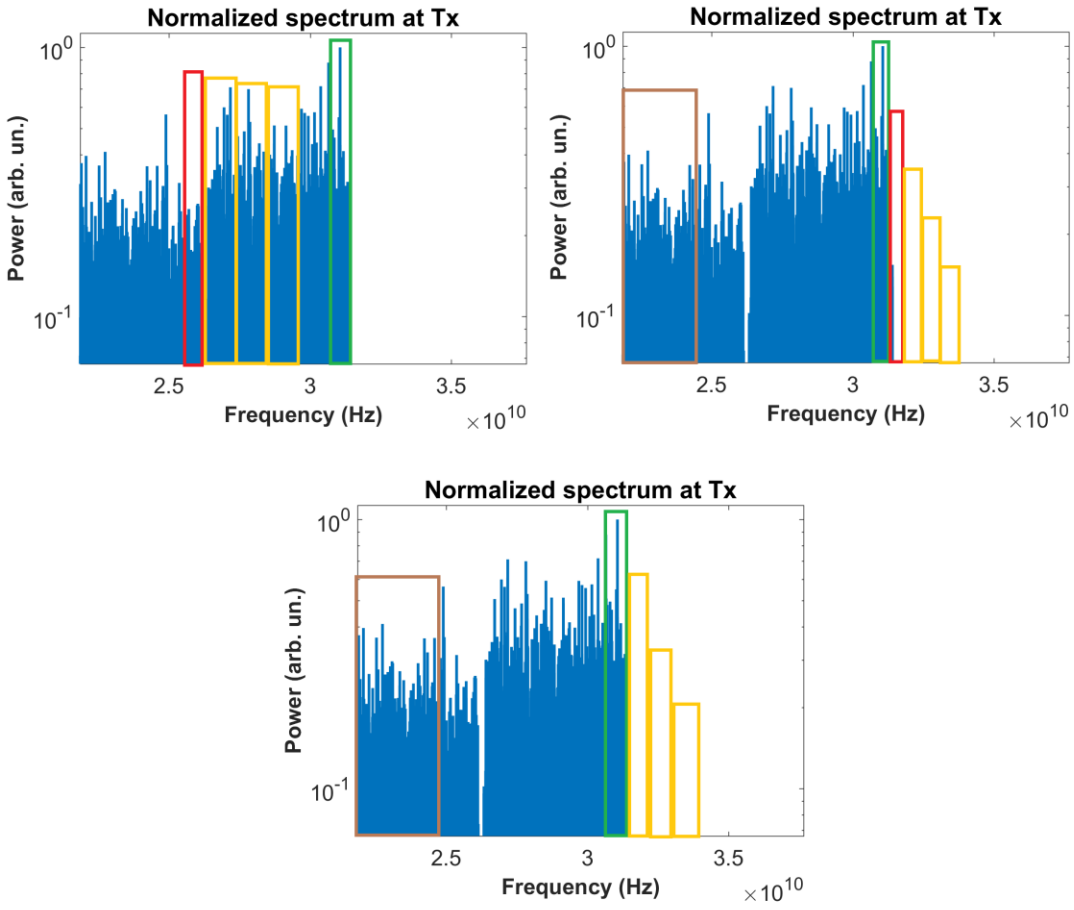

Fig. 3.6: Underestimation, overestimation and correct detection of blocks.

We must then look at each sample around this chosen block, as the block itself would just give a rough estimate of where the edge frequency is. For example, if the detected block was number 56 in our 4000 samples (80 blocks) window, we multiply 56 by 50 as there are 50 samples per block. This corresponds to the 2800th sample. We then take +/- 50 samples centered on this sample (2751-2850), forming a new smaller window. It should be evident now that because we are now taking a +/- 50 samples window around the detected block's first sample, it does not matter if we are off by one block when obtaining the rough estimate. After this new smaller window is taken, we start from the first sample and take it to be our initial maximum value. We then compare the second sample with the first. If the power of the second sample is greater than some threshold value, 0.7 in our case, we replace the old maximum sample number with the new one. We continue this process until we reach the end of this window. The correct edge frequency is now found by adding this value to the starting sample of the detected block's frequency. For example, if the sample we found that passes our threshold test is at sample number 61, and the 58th block was the detected block, the correct frequency would be the (58*50 + (61-50)) = 2811 value in our original window. We must subtract 50 from 61 because we are taking a window centered at 2800, so the first sample would correspond to sample number 2751. An example of this process is shown in Fig. 3.7.

For detecting the edge of the received signal, we start in a similar manner, but take a larger window of 6000 samples centered around 30 GHz. This is to accommodate for the frequency fluctuation of the laser used for producing the carrier wave. Then we break this window into blocks of 50, and average their power again. Because the received signal will have a lower SNR after going through the fiber, the edge of the PSD spectrum will not be as sharp. Therefore we did not use the exact same method as just described above, though it is similar. Instead, we compared the ratio of each block (block remains 50 samples) in the 6000 sample window with another one several over in frequency. In this experiment, a difference of 6 blocks was used. This would mean the first block is

compared with the seventh, the second with the eighth, and so on. The reasoning is that the ratio of the correct block should have the highest ratio between it and the block used for comparison, as the spectrum's power attenuates after the edge. Again, because of the loss in sharpness of the received signal's PSD, this proved to be a more robust method of determining the estimate for the received spectrum's edge. Using this estimate we can then get a general idea of where the true edge is.

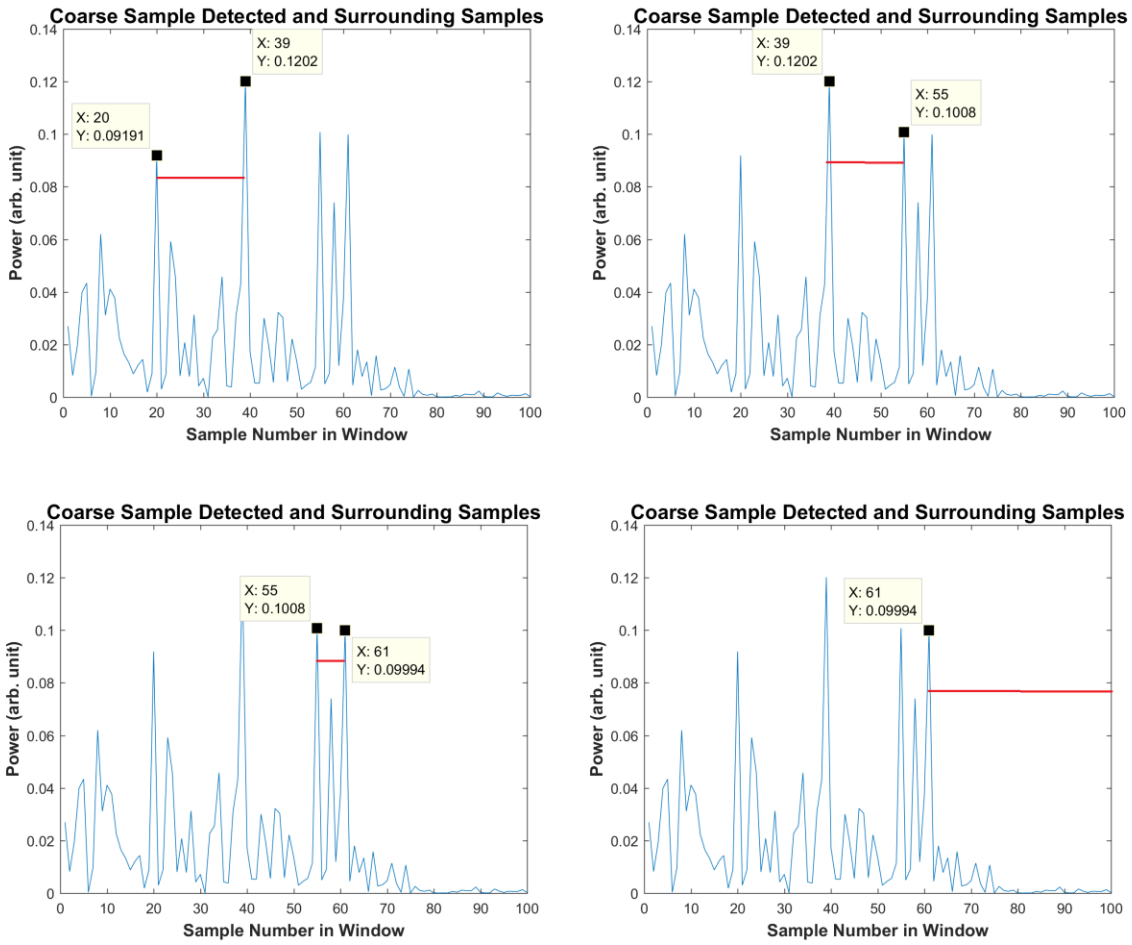

Fig. 3.7: Example of threshold test.

3.4.2 Array Setup

With the correct edge for the transmitted signal and a rough estimate for the edge of the received, we can obtain a good estimate for where the IF offset should be by using

$$IF_{Offset} = FreqEdge_{Tx} - FreqEdge_{Rx}, \tag{3.6}$$

Because this is a rough estimate, instead of using the value calculated in (1), we take a window centered around the calculated value as the range of possible frequencies. For our experiment, a window of +/- 150 MHz was taken. A smaller window and the correct frequency may not be detected, whereas a larger window would likely take more computations to detect the correct frequency. As an example, for a TX edge frequency of 30 GHz and an RX edge frequency of 30.3 GHz, the estimated IF offset would be -300 MHz. We then take a range of frequencies around this estimate—i.e.-450 MHz to -150 MHz. An example of this smaller window is shown in Fig. 3.8.

We then form a second array from this first array, by sorting the elements in order of decreasing power. This is done as from (much) empirical evidence it was seen that, in almost all cases, the correct edge frequency would lie at or next to a local peak in the spectrum, with the largest peaks more likely to be the correct value (similar to how the Tx. edge frequency was taken at a local peak in Figure 4). By using a range of frequencies, it can also be seen here that even an incorrect detection of the TX or RX edge frequency can still lead to the correct IF offset, although there would most likely be more computations needed. It is also possible to form the second array by utilizing only the local peaks of the first array, and then sort these peaks in order of decreasing power. Again, this is due to the edge most likely lying near a local maximum, therefore removing unnecessary frequency points. This made the processing faster on average, though in a few cases the correct IF offset could no longer be detected. Therefore, we first used this reduced array consisting of only local peaks, and if the IF offset was not found, we redid it using the full array.

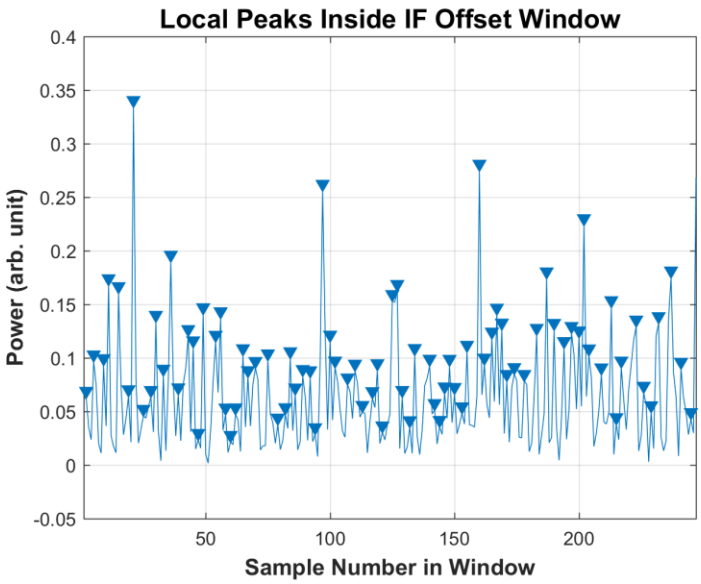

Fig. 3.8: Using only local peaks inside IFO window can greatly speed up algorithm.

3.4.3 Estimation Verification

Starting from the first index of the sorted power array, we take its value and search for the same value inside the unsorted array (the sample with the largest power in Figure 5). Once it is found, we take the index corresponding to that term and use it to obtain the estimated IF offset. For example, in a window of -450 MHz to -150 MHz, if the index with the largest power corresponded to the 100th element in the window, then the estimated IF offset would be -350 MHz, assuming each sample is spaced 1 MHz apart. We can now shift the spectrum by this frequency, giving us our first estimation point.

For each subcarrier in the MSC system, we start by converting the signal down to baseband by shifting the frequency with the appropriate amount for that subcarrier. Here we also take a portion of the known transmitted data and do the same procedure of converting to baseband. For our experiments 10000 samples of transmitted data were taken out of a total of 98304, although in

most cases 5000 samples were sufficient. We then filter the received signal and the training sequence of the transmitted signal using a root-raised cosine filter. We can also then downsample to 2 samples/symbol for quicker processing, giving us 4096 samples for each subcarrier of received data and 833 samples for each subcarrier of transmitted data.

We then take the XC between the downsampled transmitted and received signals. For each subcarrier, we save the index corresponding to the maximum of this XC calculation in another array (XCArray). The timing shift between two channels is given by

$$\Delta T = 2\pi \Delta f \beta_2 L, \tag{3.7}$$

where Δf is the channel spacing, β2 is the group velocity dispersion parameter and L is the length of the fiber. Because the subcarriers are closely spaced together in MSC, only a small timing shift exists between all subcarriers. Therefore, , the values inside the XCArray should be the approximately, as the subcarriers are closely spaced together. If this is the case, we know that the correct IF offset value was chosen, as it would be extremely unlikely that an incorrect IF offset value could produce a result of multiple subcarriers with identical peaks

$$\text{Probability of Incorrect Decision} = \frac{1}{\text{N Choose K}}, \tag{3.8}$$

Here we are using a combination where N is the number of samples in the signal and K is the number of subcarriers. For our case of 4096 samples and 12 subcarriers, the probability of an incorrect frequency giving a correct result is around 4.5e-44, therefore we can assume that this verification is valid. The different subcarriers should have a similar index value for the maximum point in the XC calculation. Therefore, we can calculate the variance of the XCArray, and that result should fall below a small threshold (we used a variance of 5 as our threshold). If the calculated variance does not fall below this threshold then we realize that the incorrect IF offset was chosen,

move on to the next element in the sorted power array and repeat the process. Once an IF offset value is chosen which produces a variance of less than 5 for the XCArray, we end the loop and choose that offset as the correct value.

Although the aforementioned verification method worked for all our test cases, there are a few potential possibilities where it may fail. Particularly, if not enough training samples are used or one subcarrier's maximum XC value is off from the rest, this may lead to a large variance even though the correct IF offset value was chosen. Therefore another backup verification method was also implemented to catch any of these errors should they arise.

After taking the XC, we save this signal for each subcarrier. After all subcarriers XCs have been calculated, we sum all of the XC signals together. The maximum value for the new, total XC (TXC) signal should have a large distinct peak if the correct IF offset was chosen, as incorrect samples can be thought of as noise, and their sum's will not form as large of a peak relative to the correct sample. An example of a distinct peak that is formed at the correct sample is shown in Fig. 3.9. We then take the ratio of this peak with the mean of the entire TXC signal. If the ratio is greater than a certain threshold, then the correct IF offset was used. A flow-chart of the frequency offset estimation algorithm is shown in Fig. 3.10.

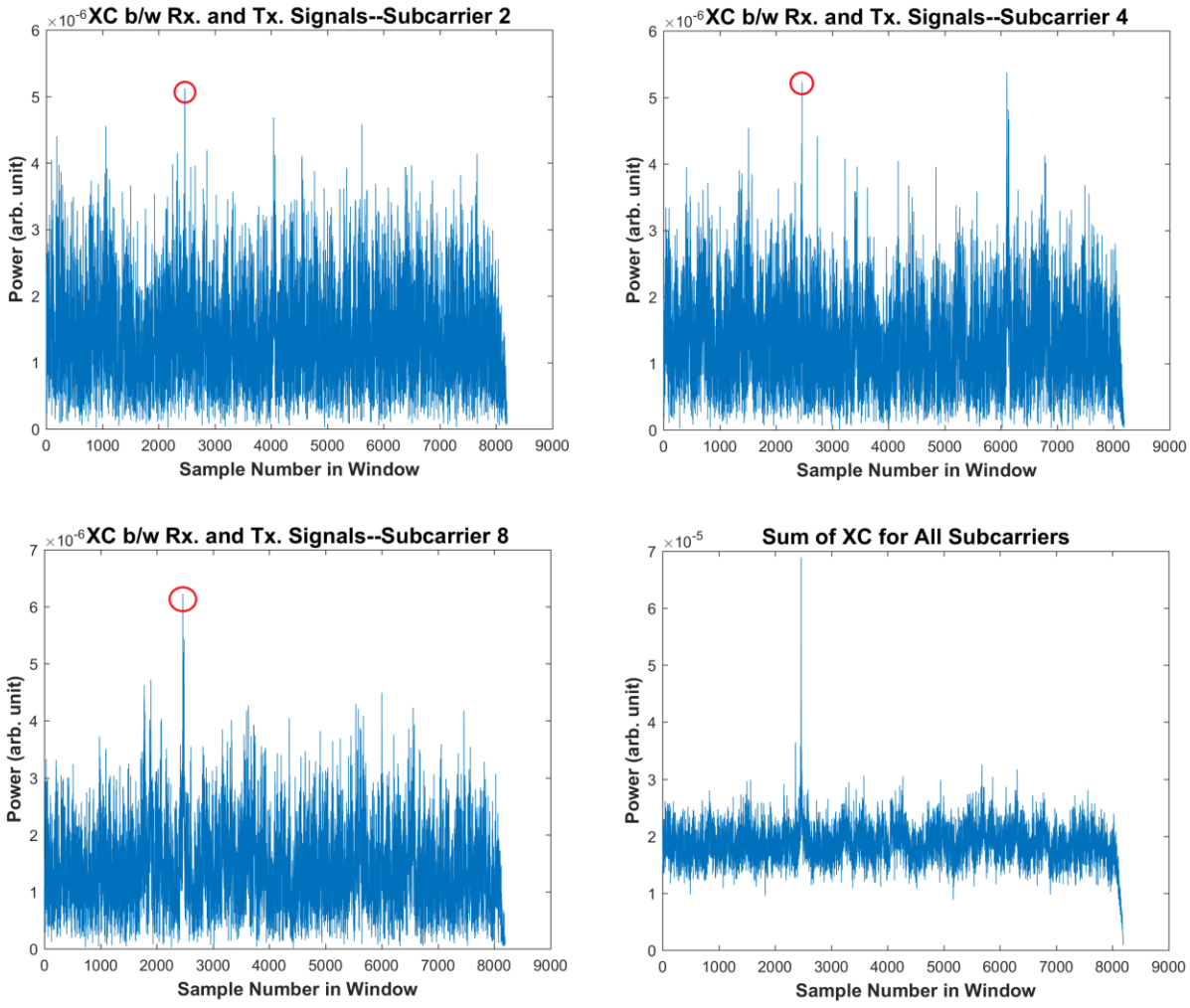

Fig. 3.9: Adding up each subcarrier's XC spectrum yields a distinct peak when the correct frequency estimate is chosen.

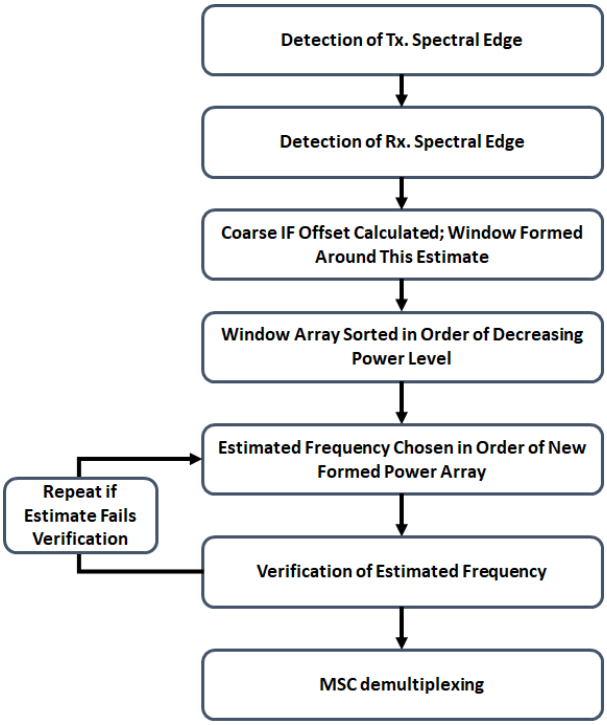

Fig. 3.10: Overview of frequency offset estimation algorithm.

3.5 Results

The results are shown below in Figs. 3.11 and 3.12. The majority of the time, the correct IF offset can be detected within the first few guesses. Although the method described above proved to be satisfactory, it should be noted compensating for chromatic dispersion prior to searching for the IF offset helped here. If we had not done this, then the XC values for each subcarrier would increase in a linear manner, instead of centering on a peak. The correct IF offset can still be found if this is the case though, by searching for which value gives this constant XC slope for the subcarriers.

Fig. 3.11 shows the Q-Factor as a function of launch power when the transmission distance is 6000 km, with DBP and CDC. As shown, the optimal launch power was found to be 4 dBm for this system, and DBP brings about 0.73 dB of performance improvement over CDC. Fig. 3.12

shows the Q-Factor as a function of transmission distance at the optimal launch power (4 dBm). As can be seen, lengths approaching 9000 km or more are allowable for this system, if soft forward error correction is used in conjunction. Finally, Fig. 3.13 shows the number of guesses needed ntilu the correct IFO to be chosen. This proves that this algorithm is an efficient means to estimate the IFO in the majority of the potential cases.

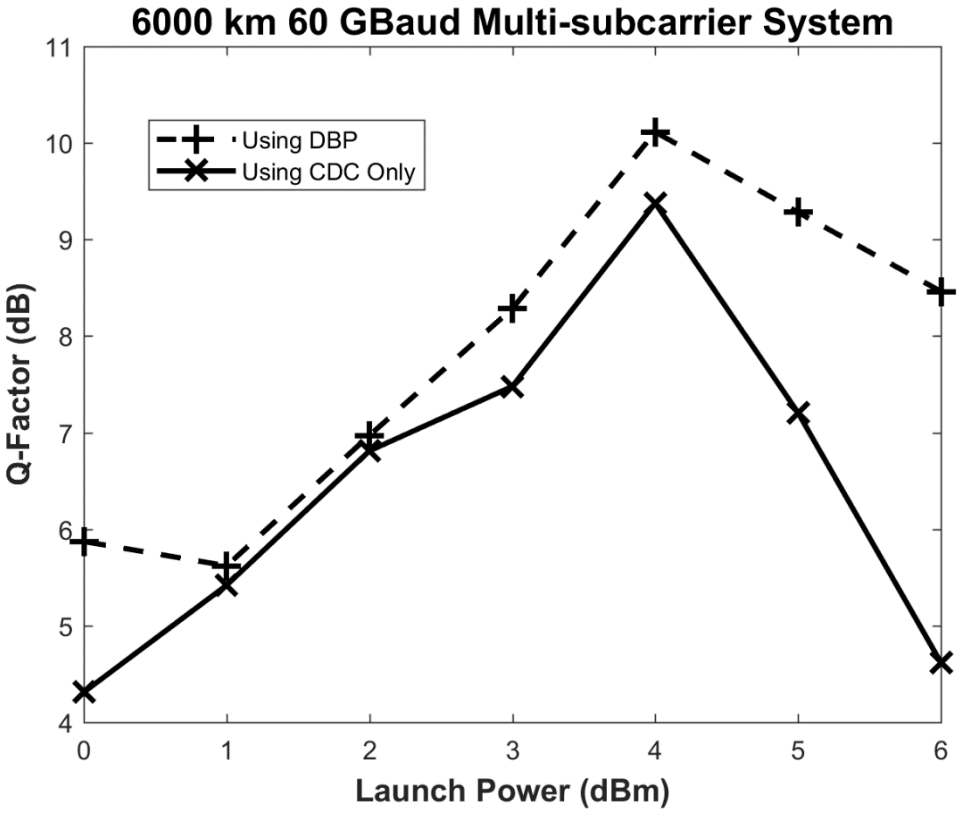

Fig. 3.11: Q-factor as a function of launch power.

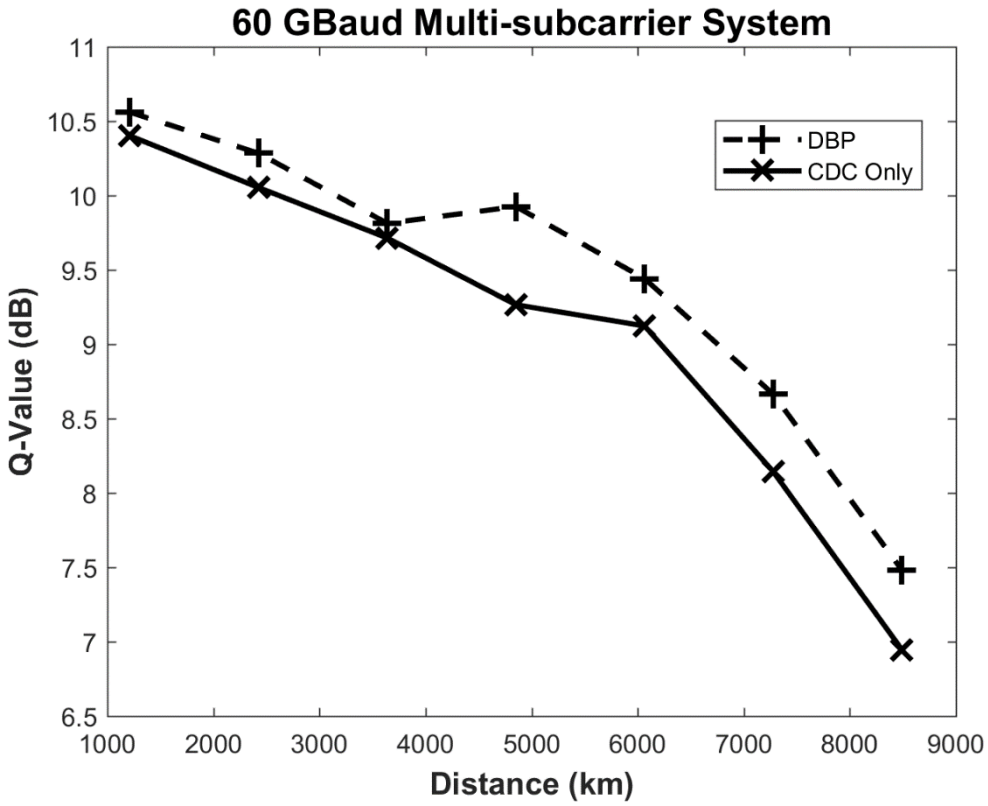

Fig. 3.12: Q-factor vs. distance at launch power of 4 dBm.

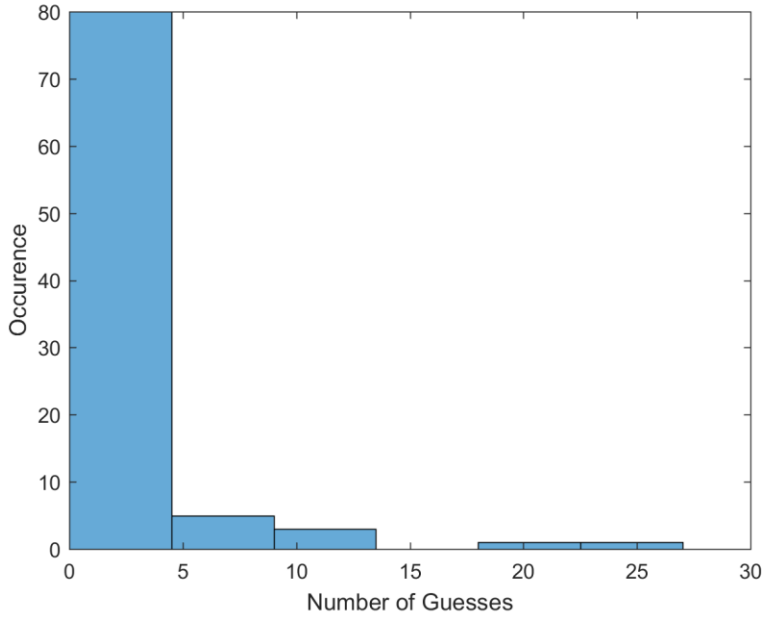

Fig. 3.13: Number of guesses needed for until correct detection.

Chapter 4

Fast Fourier Transform Based Processing

This chapter introduces a more efficient way to generate MSC signals, by making use of the well-known Fast Fourier Transform (FFT) algorithm. Traditional based MSC techniques have a computational complexity that scales in the order of $O(N_c^2)$. The proposed FFT method's computational complexity scales in the order of $O(M \cdot N_c \cdot \log_2(2 \cdot N_c))$ though, where N_c is the number of subcarriers and M is the number of samples per second. This technique therefore becomes a more enticing alternative as the number of subcarriers increases, which is an emerging trend as larger baud rate systems become deployed.

4.1 Need for FFT-Based Processing

Traditionally, to generate MSC signals an excessive number of samples needs to be generated. Due to the multiplexing of the subcarriers, each subcarrier must be oversampled by a factor proportional

to the number of subcarriers being used. For example, the bandwidth of a MSC signal is proportional to the number of subcarriers, N_c, and therefore, the number of samples per symbol is proportional to N_c. The modulation process involves the multiplication of each subcarrier by a complex sinusoid and hence, the required complex multiplication per symbol scales as $O(N_c^2)$. Thus as the number of subcarriers increases, the computational cost makes generating MSC signals more and more impractical, as the cost-per-bit (CPB) increases quadratically. Therefore, to take advantage of the benefits MSC signals bring, while still keeping them as a realistic option for commercial applications, a more efficient technique for generating these MSC signals is needed which reduces the CPB. Such a technique is proposed here.

We do this by dividing the signal into blocks and in each block we transform the signal in such a way that it corresponds to a signal that can be represented by the Discrete Fourier Transform (DFT). With the signal in this format, we are able to use the FFT algorithm for faster signal processing, as it uses fewer computations than the DFT while yielding the same result. The computation cost of the FFT signal scales as $O(M \cdot N_c \cdot \log_2(2 \cdot N_c))$, thereby giving an increase in CPB savings compared with the traditional method, as the number of subcarriers increases. A similar computational saving can be shown when demultiplexing the signal at the receiver.

Recently, superchannels with baud rates up to 120 GBaud per channel have drawn significant interest. As the trend of operating at larger system baud rates is likely to continue for the foreseeable future, this method of generating MSC signals and the savings that it brings can have a greater impact, as MSC become an even more enticing option at larger system baud rates, while also having more subcarriers at these baud rates.

Although it may appear that the proposed technique resembles orthogonal frequency-division multiplexing (OFDM), these two techniques are quite different. Firstly, in this approach, the carriers are not orthogonal. Secondly because as RRC pulses decay slowly, at a given symbol interval

the symbols corresponding to the neighboring intervals interfere strongly. In contrast, OFDM symbols do not typically interfere and there is a guard interval between symbols. The purpose of the FFT in this approach is only to reduce the computational complexity.

4.2 Theory

4.2.1 MSC Transmitter

A baseband signal modulating a single carrier can be represented as

$$s_m(t) = \sum_{n=-Ns/2}^{Ns/2-1} a_n^{(m)} p(t - nT_s), \tag{4.1}$$

where $a_n^{(m)}$ is the data on the m^{th} subcarrier and n^{th} symbol period, T_s is the symbol interval, and $p(\cdot)$ is the pulse shape function. We assumed that $p(t)$ correspnds to root-raised cosine (RRC) filtering with a rolloff factor a. pulse in this thesis. After multiplexing, the signal is given by

$$s_{total}(t) = \sum_{m=-Nc/2}^{Nc/2-1} s_m(t) \exp(i2\pi f_m t), \tag{4.2}$$

where f_m is the center frequency of the m^{th} subcarrier. We assume that the subcarriers are uniformly spaced with a subcarrier spacing Δf_{sc} i.e.

$$f_m = m\Delta f_{sc}. \tag{4.3}$$

The analog signal in (1) is discretized with M samples per symbol period

$$\Delta t \equiv \frac{T_s}{M}, \tag{4.4}$$

where Δt is the sampling period in the baseband. The bandwidth of the signal modulating each subcarrier is $B_s \cdot (1+2)/2$, where $B_s = 1/T_s$. In order to avoid spectral overlap between the subcarriers, let the subcarrier spacing be

$$\Delta f_{sc} = B_s(1+\alpha)\,. \tag{4.5}$$

The total bandwidth of the MSC signal is then $N_c \cdot B_s \cdot (1+\alpha)$, and by using the Nyquist sampling rate, the chosen sampling rate will be twice that, or $2 \cdot N_c \cdot B_s \cdot (1+\alpha)$, and the sampling period is

$$\delta_t = \frac{T_s}{2N_c(1+\alpha)} = \frac{M\Delta t}{2N_c(1+\alpha)}\,, \tag{4.6}$$

$$N_c' = \lfloor N_c(1+\alpha) \rfloor, \tag{4.7}$$

where $\lfloor \cdot \rfloor$ denotes the floor function of rounding down to the nearest integer.

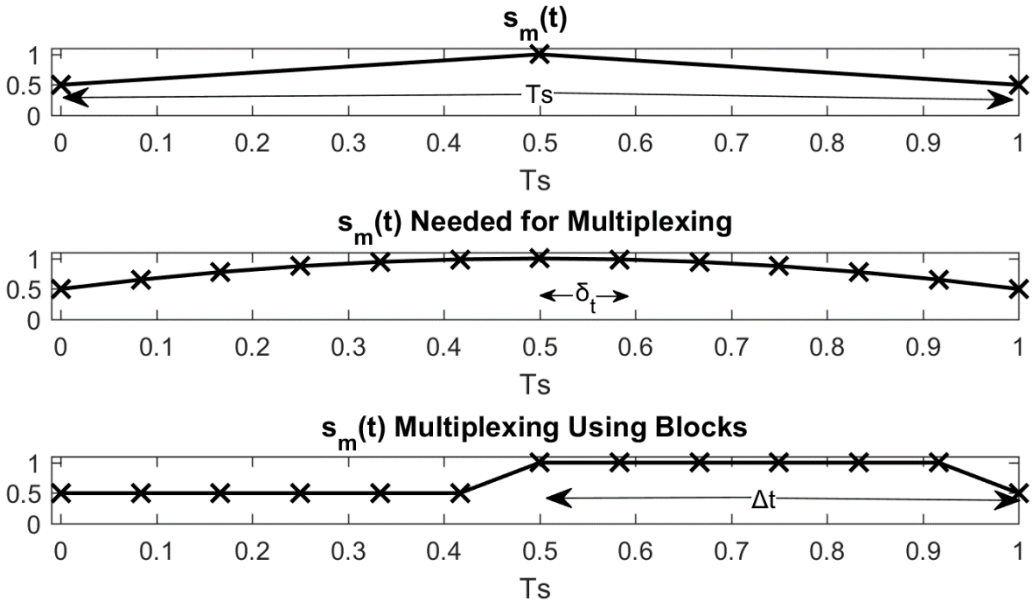

Fig. 4.1: Constant sampling over a block can be used to represent signal needed for multiplexing. Each block is equal to the number of subcarriers, 6 in this example.

As can be seen in the bottom graph in Fig. 4.1, $s_m(t)$ is constant over a time period $N_c' \cdot \delta_t$, and we can divide the time vector into blocks of size Δt. Let $s_m(t)$ be a constant, $s_m^{(j)}$, in j^{th} block. Eq. (4.2) is processed separately for each block. Consider a block j with $(j-1)\Delta t \leq t < j\Delta t$. This block has N_c' elements in it. Let k be the index to address these elements. The time vector t is then discretized within

this block as

$$\begin{aligned} t &= (j-1)\Delta t + k\delta_t \\ &= \ell\delta_t \end{aligned}, \tag{4.8}$$

where

$$\ell = (j-1)\frac{2}{M}N_c(1+\alpha)+k, \tag{4.9}$$

and

$$0 \le k < N_c'. \tag{4.10}$$

It can then be shown that

$$\Delta f_{sc}\delta_t = \frac{1}{2N_c}. \tag{4.11}$$

Now, we process Eq. (4.2) so that it can be computed using the FFT, via changing the format of the signal to that which can be represented by a DFT. Using Eqs. (4.8), (4.9) and (4.11) for the j^{th} block, the exponential term in Eq. (4.2) may be written as

$$\begin{aligned} i2\pi f_m t &= i2\pi m\Delta f_{sc} l\delta_t \\ &= i\frac{2\pi m}{2N_c}\left[(j-1)\frac{2}{M}N_c(1+\alpha)+k\right]. \end{aligned} \tag{4.12}$$

Substituting Eq. (4.11) into (4.2) yields

$$s_{total}(l\delta_t) = \sum_{m=-Nc/2}^{Nc/2-1} s_m'^{(j)} \exp\left(\frac{i2\pi mk}{2N_c}\right), \tag{4.13}$$

where

$$s_m'^{(j)} = s_m^{(j)} \exp\left[\frac{i2\pi m}{M}(j-1)(1+\alpha)\right]. \tag{4.14}$$

In Eq. (4.13), the denominator in the exponent is $2\cdot N_c$, but the summation only extends from $-N_c/2$ to $N_c/2$ -1. To express Eq. (4.13) as a DFT, we introduce virtual carriers carrying no data, i.e. rewrite Eq. (4.13) as

$$s_{total}(l\delta_t) = \sum_{m=-Nc}^{Nc-1} \bar{s}_m^{(j)} \exp(\frac{i2\pi mk}{2N_c}), \tag{4.15}$$

where

$$\bar{s}_m^{(j)} = s_m'^{(j)} \text{ for } \frac{-N_c}{2} \le m \le \frac{N_c}{2} - 1 \\ = 0 \text{ otherwise} \tag{4.16}$$

Eq. (4.15) can be evaluated using FFT. The number of complex multiplications to evaluate it is $(N_c/2)\cdot\log_2\cdot(2\cdot N_c)$. In contrast, if the FFT is not used, evaluation of (11) requires N_c^2 complex multiplications. When RRC pulse is used, $M \le 2$, and hence the computational cost of the evaluation of Eq. (4.15) using the FFT is much less than that of Eq. (4.13), as the number of subcarriers grows larger than $N_c > 8$. Additional N_c complex computations are needed per block for evaluating Eq. (4.13), which becomes negligible as N_c grows.

A block diagram up until this point is shown in Fig. 4.2. The output of the FFT operation on each block gives the multiplexed data that we are interested in. There are an additional N_c outputs due to the addition of the virtual subcarriers, however we only need N_c values for each block. The chosen points will depend on where the real subcarriers are placed before performing the FFT.

Once the unnecessary data is eliminated (which is present due to the virtual subcarriers), we can form the final transmitted signal by concatenating the blocks into a single vector. The first N_c samples, 1 to N_c, for this vector will correspond to the first block's data, the second N_c samples, N_c+1 to $2N_c$, with the second block, and so on.

The complex electrical signal modulating the optical carrier $s_{tr}(t)$ is shown to be

$$s_{tr}(t) = s_{total}(t)\exp(i\pi\Delta f_{sc}t). \tag{4.17}$$

The frequency shifting down here is needed due to the FFT operation not being centered perfectly around 0. It is needed if the total number of subcarriers is an even integer—which is always the case

since we double the amount of subcarriers when adding in the virtual subcarriers. This adds an additional amount of complex computations equal to the signal's length, i.e. $N_s \cdot M \cdot N_c$, however for a large number of subcarriers this term becomes negligible too.

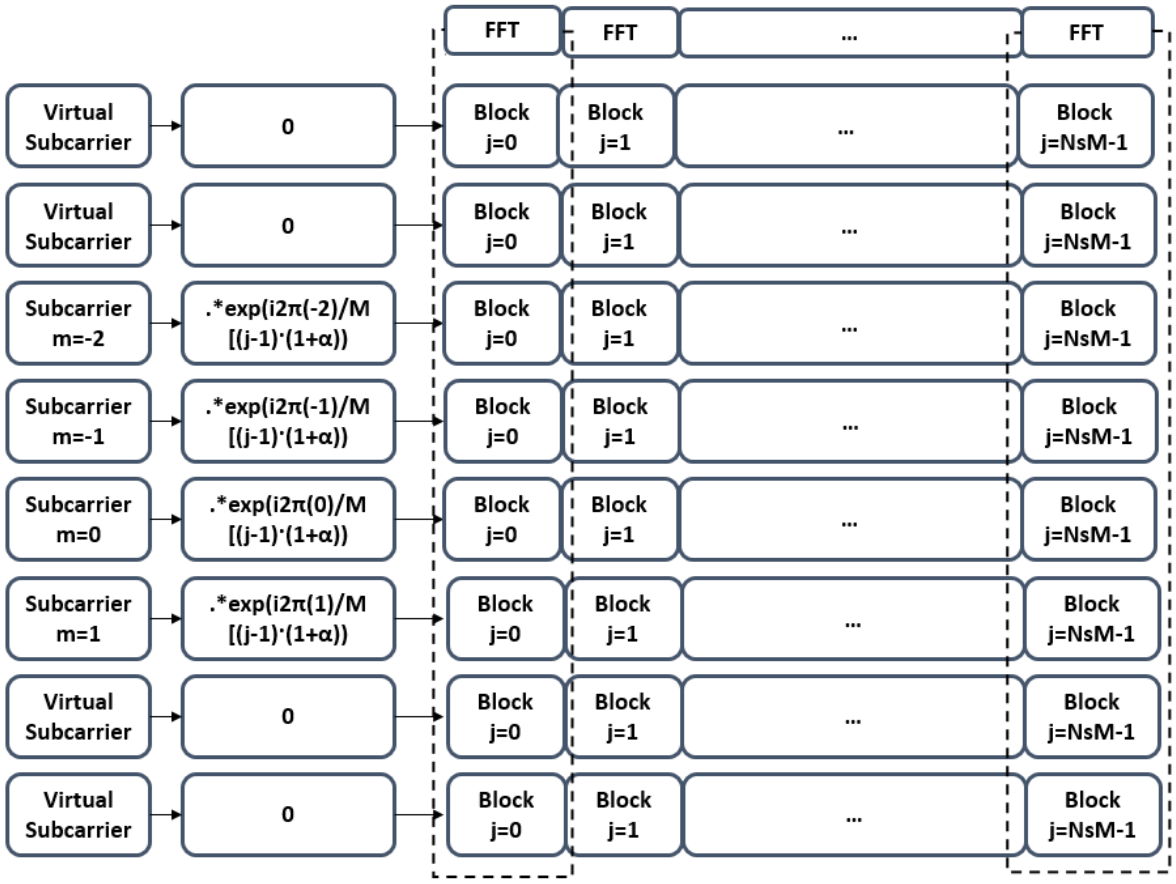

Fig. 4.2: Block diagram of transmitter side using FFT method using four subcarriers (Nc=4) and two samples per symbol (M=2).

The total computation cost of evaluating Eq. (4.2) using the FFT technique is $M \cdot N_s \cdot [(N_c/2) \cdot log_2 \cdot (2 \cdot N_c) + 2N_c]$, where $M \cdot N_s$ is the number of blocks. When evaluating Eq. (4.2) without the FFT, the number of computations is $2 \cdot N_s \cdot N_c^2$. Table 1 compares the number of complex multiplications required for evaluating Eq. (4.2) with and without the FFT. As the number of subcarriers increases, the proposed approach provides significant computational cost savings. Even

when the number of subcarriers is 8, the FFT-bases approach provides a computational cost savings by a factor of ~2.

Subcarriers	Complex Computations	
	Without FFT	With FFT
4	131072	114688
8	524288	262144
16	2.10E+06	589824
32	8.39E+06	1.31E+06
64	3.35E+07	2.88E+06
128	1.34E+08	6.29E+06

Table. 4.1: Comparison between the two approaches at the transmitter side using M=2 samples per symbol and Ns=4096 symbols.

4.2.2 MSC Receiver

Let the received signal after dispersion compensation be $s_{rec}(t)$. In the absence of fiber nonlinear effects

$$s_{rec}(t) = s_{tr}(t) + n(t), \tag{4.18}$$

where $n(t)$ is the noise added by the channel. To make use of the FFT at the receiver, we first must shift the received signal to undo the shift done in (15), allowing the signal to get back into an FFT structure.

$$s'_{rec}(t) = s_{rec}(t)\exp(-i\pi\Delta f_{sc}t). \tag{4.19}$$

This signal, of length $1xN_c$, is fragmented into $M \cdot N_s \cdot N_c$ blocks. The first N_c samples of $s'_{rec}(t)$ correspond to the first block, the second N_c samples, N_c+1 to $2N_c$, with the second block, and so on. We call these blocks $\mathbf{s}'^{(j)}_{m\_rx}$, with j indicating the block number.

Similar to the transmitter, the introduction of virtual subcarriers is needed to create a DFT structure. This gives us the following equations

$$\bar{s}_{m\_rx}^{(j)} = s_{m\_rx}^{\prime(j)} \text{ for } \frac{-N_c'}{2} \le m \le \frac{N_c'}{2} - 1, \quad = 0 \text{ otherwise} \tag{4.20}$$

$$s_{rx}^{(j)} = \sum_{m=-Nc}^{Nc-1} \bar{s}_{m\_rx}^{(j)} \exp\left(\frac{-i2\pi mk}{MN_c}\right). \tag{4.21}$$

After the FFT operation we must compensate for Eq. (4.13), which is done by

$$s_{rx\_final}^{(j)} = s_{rx}^{(j)} \exp\left[\frac{-i2\pi m}{M}(j-1)(1+\alpha)\right] \tag{4.22}$$

Finally, $s_{rx\_final}^{(j)}$ is then passed through a RRC filter to complete the demultiplexing process (see Fig. 4.5). After the matched filter, the data in each subcarrier is processed in parallel. Similar to the transmitter section, the operations in Eqs. (4.19) and (4.22) add additional $Ns \cdot M \cdot Nc$ complex computations each. The computational cost of the demultiplexing using this technique is $M \cdot N_s \cdot [(N_c/2) \cdot \log_2 \cdot (2 \cdot N_c) + 2N_c]$, yielding similar savings as the receiver compared with the traditional method.

4.3 Simulations

Fig. 4.3 shows the schematic of the fiber optic system based on the proposed MSC processing using the FFT. Figs. 4.4 and 4.5 show the details of this FFT-based MSC processing at the transmitter side and receiver sides, respectively.

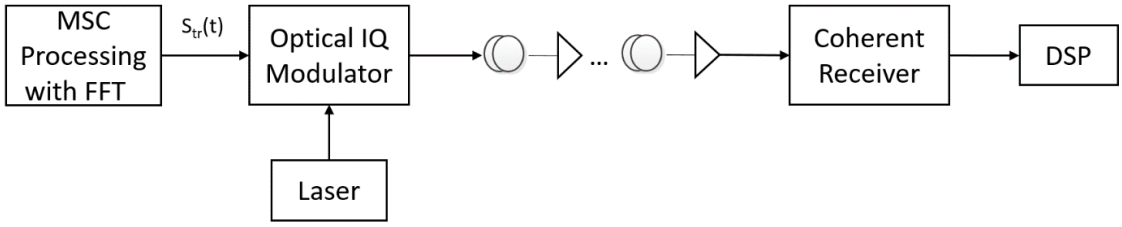

Fig. 4.3: Overview of fiber system used in simulations.

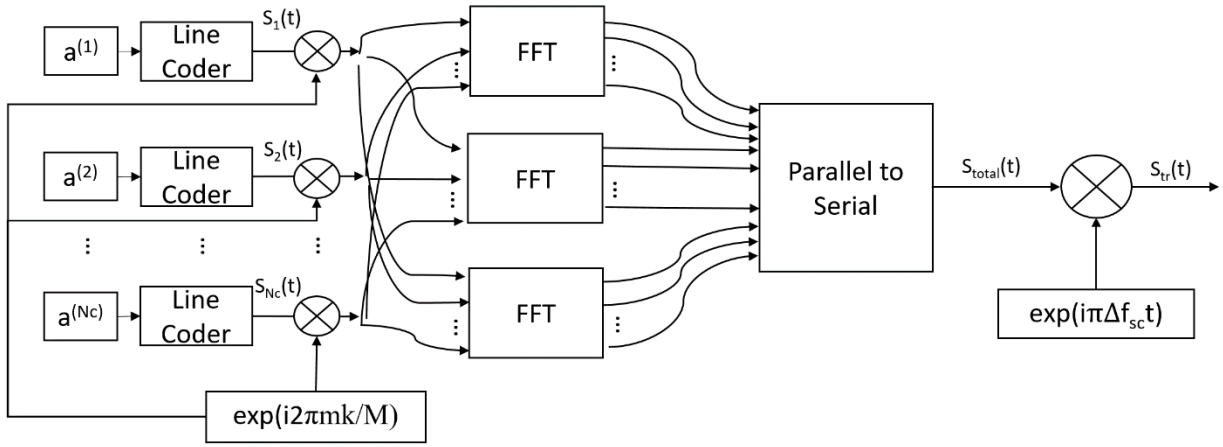

Fig. 4.4: Overview of transmitter side DSP.

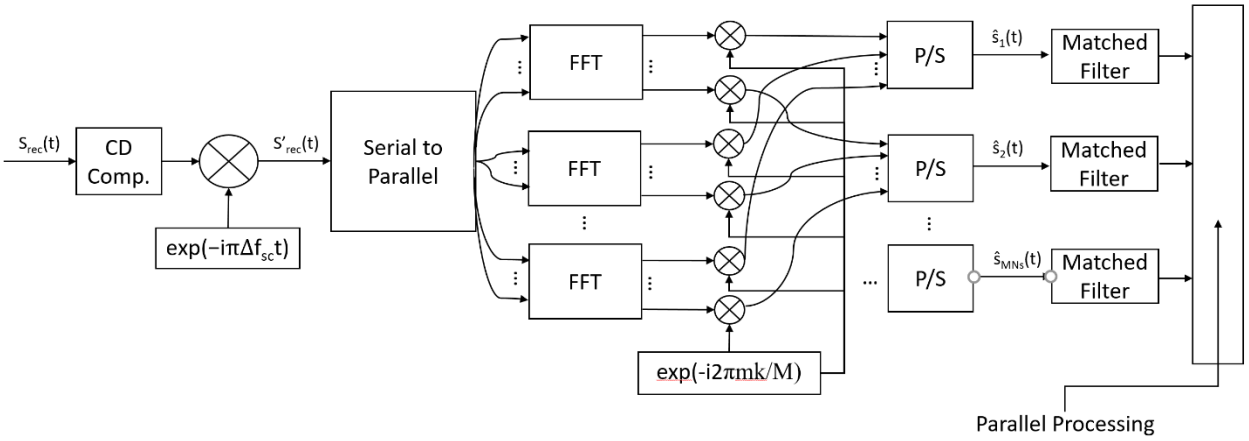

Fig. 4.5: Overview of receiver side DSP.

We simulate a dual-polarized 60 GBaud system using QPSK data on each subcarrier. The fiber spans had lengths of 101 km, with 17.82 dB average span loss. The dispersion parameter was 21 ps/(nm·km), and 125 μm^2 effective area. The noise figure of the amplifier was 5.26 dB. 100 kHz linewidths were used at both the transmitter and local oscillator. The signal propagation in the fiber is simulated using the well-known split-step Fourier technique.

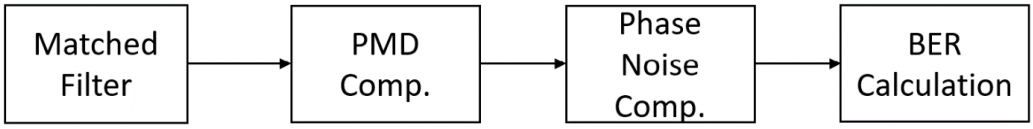

Fig. 4.6: Parallel processing of each subcarrier.

The number of symbols in each carrier was 4096 at 2 samples per symbol. The RRC filtering with a rolloff factor of 0.05 was used. The received signal passes through the proposed FFT-based demultiplexer and after the matched filter, the data on each subcarrier passes through a PMD compensation and phase noise compensation stage. The phase noise compensation is implemented using the popular Viterbi-Viterbi algorithm. The mean BER of all the subcarriers is computed by error counting and the Q-Factor is calculated using

$$Q = 20\log_{10}(erfcinv(2\times BER)\times\sqrt{2}), \tag{4.23}$$

where erfcinv is the inverse error function. Fig. 4.7 shows the Q-Factor as a function of fiber launch power when the transmission distance is 8000 km. A launch power of 4 dBm was found to be ideal for both the traditional method and the FFT method. Fig. 4.8 shows a comparison of the two techniques at varying lengths at a launch power of 4 dBm. 16 subcarriers were used. As can be seen, the results when using the FFT technique gives similar results to that of the traditional method, while taking advantage of the computational costs the FFT brings, thus lowering the CPB.

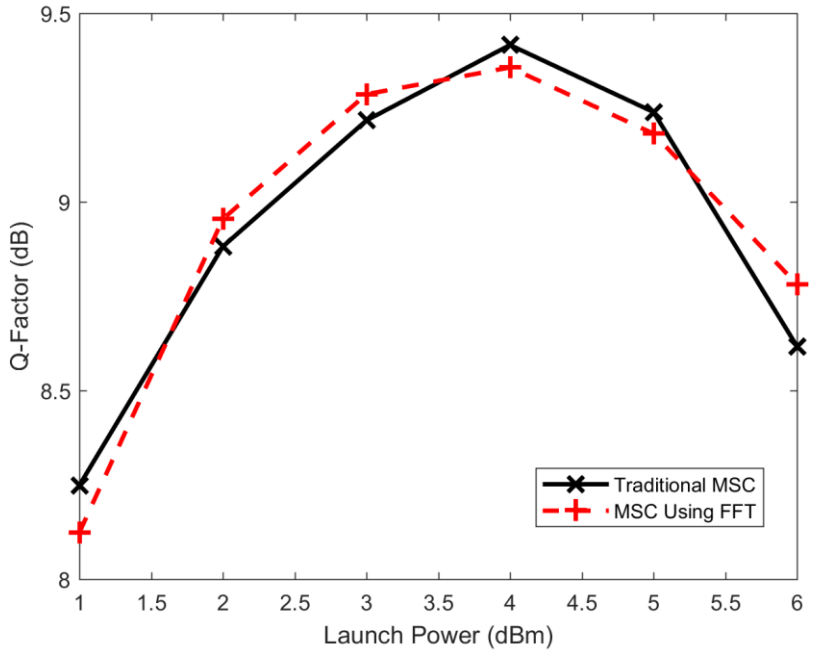

Fig. 4.7: Q-Factor for different launch powers shown.

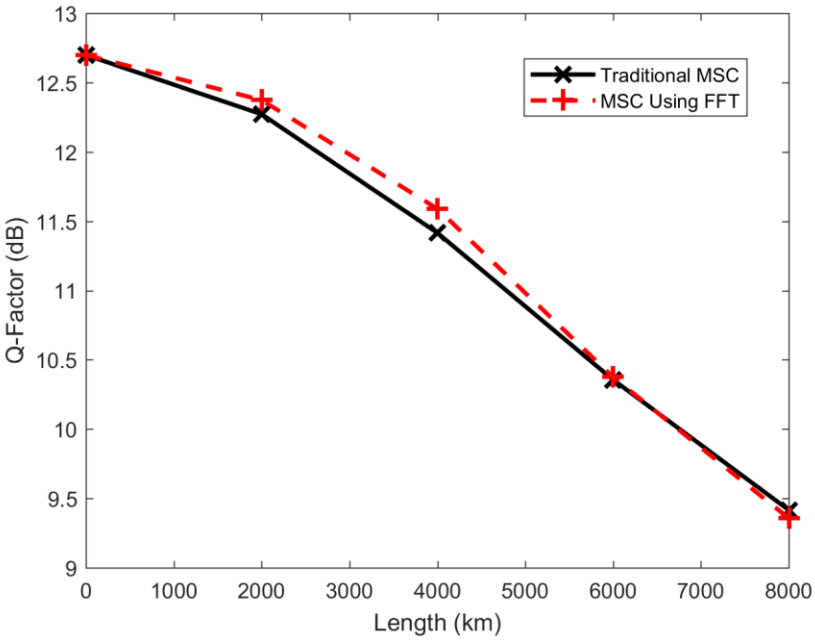

Fig. 4.8: Simulation results at varying length at a launch power of 4 dBm.

Fig. 4.9 shows the computation time of the transmitter side DSP with and without FFT processing. The simulations is carried out on Matlab R2017a on and Intel® Core™ i7-7700HQ CPU @ 2.80 GHz, 2801 MHz, 4 Cores, 8 Logical Processors. Consistent with Table 1, there is a significant reduction in computational time using the proposed FFT based approach when the number of subcarriers is large. For example, when the number of subcarriers is 64, the computational time decreases by a factor of ~100 for the FFT based technique. Fig. 4.9, as well as Table 4.1, includes the computations required for setting up the FFT structure as well. This gives further proof that the FFT-based approach is an improvement to the traditional method.

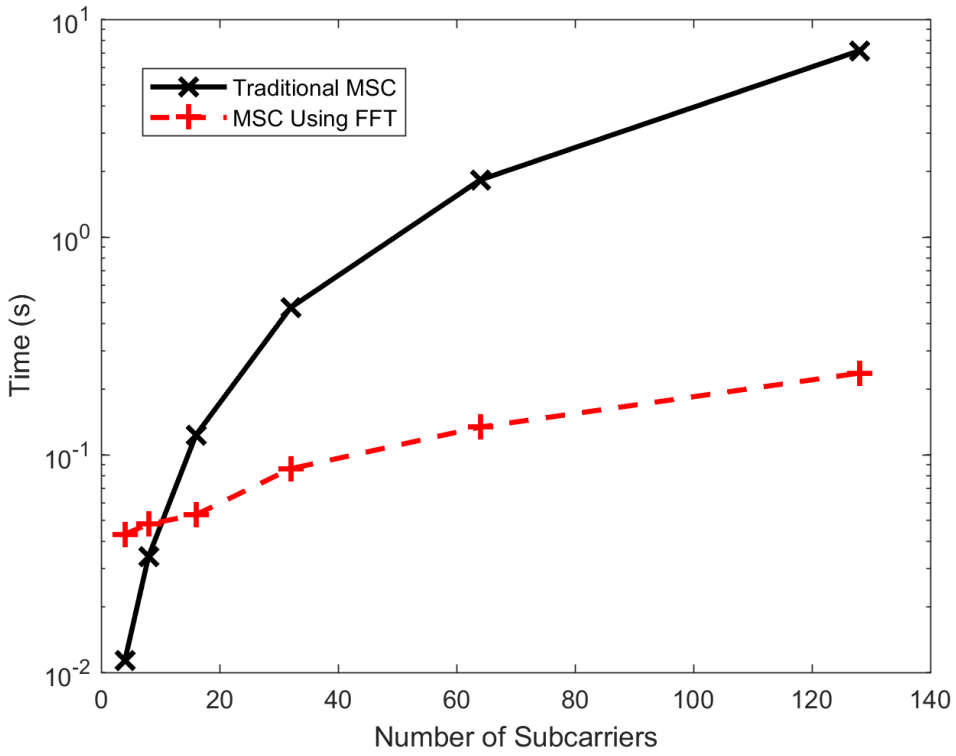

Fig. 4.9: Comparison for transmitter when using M=2 samples per symbol and Ns symbols while varying the number of subcarriers.

Chapter 5

Conclusion

Fiber optic communication systems are essential for contemporary living standards. Due to the high frequency and in turn the large bandwidth these systems occupy, enormous amounts of data are enabled to be transferred at a time. With this said, there are still challenges which are needed to be overcome for the continued growth. In Chapter 2 an explanation pertaining to why nonlinear impairments, one of the main obstacles optical fibers face today, are formed. Multi-subcarrier signal processing, which breaks up a large carrier into several smaller carriers, was shown to be an effective solution to reduce these detrimental nonlinear effects. It works by finding and operating at an optimal point for mitigating these effects.

To make use of this new scheme though, some of the signal processing techniques that work for single carrier systems have to be altered. Removing the intermediate frequency offset—an unavoidable effect for coherent systems—is one such algorithm that has to be modified if we are to reap the benefits of multiple subcarriers. In Chapter 3 such an algorithm was proposed. Here, we

showed that by correctly detecting the edges of both the receiver and transmitter spectrums, the difference between these two parameters could be shown to be the value we are seeking. By using the cross-correlation between the received data and a subset of the transmitted data, we are then able to verify whether the correct estimate was chosen, and if not, iterate by updating the estimate until the correct value is chosen.

Although multi-subcarrier systems allow us to reduce the total amount of nonlinearities in a system, the computational costs to produce them remained high, thus potentially making them impractical for commercial systems. In Chapter 4, a new method to produce these signals was introduced. By first rearranging the subcarriers so that they can be represented by the discrete Fourier transform, we can then make use of the fast Fourier transform to generate the signal. This greatly reduces the computational costs required, especially as the number of subcarriers grows, allowing multi-subcarrier systems to become a practical solution to reducing nonlinear penalties.

Although multi-subcarrier signal processing can not solve all the problems fiber-optic communication systems face, they are a viable solution for a class of problems. This holds even further true for long-haul systems. Thus, as multi-subcarrier signal processing is a solution which aids optical fibers in meeting the ever-growing capacity demand placed on them, it should be enthusiastically accepted.

Bibliography

[1] K. C. Kao and G. A. Hockham, "Dielectric-fibre surface waveguides for optical frequencies," in Proceedings of the Institution of Electrical Engineers, vol. 113, no. 7, pp. 1151-1158, July 1966.

[2] T. Miya, Y. Terunuma, T. Hosaka and T. Miyashita, "Ultimate low-loss single-mode fibre at 1.55 μm," in Electronics Letters, vol. 15, no. 4, pp. 106-108, 15 February 1979.

[3] S. Kumar and M.J. Deen, "Fiber Optic Communications: Fundamentals and Applications", Wiley Inc., London, 2014.

[4] Fatih Yaman, Neng Bai, Benyuan Zhu, Ting Wang, and Guifang Li, "Long distance transmission in few-mode fibers," Opt. Express 18, 13250-13257 (2010).

[5] Louvros, Spiros & Fuschelberger, David. (2013). "VLC technology for indoor LTE planning". 21-41. 10.1007/978-3-319-00663-5-2.

[6] "Fiber Characterization Testing For Long Haul, High Speed Fiber Optic Networks:" The FOA Reference For Fiber Optics - Testing - Chromatic Dispersion and Polarization Mode Dispersion, www.thefoa.org/tech/ref/testing/test/CD_PMD.html.

[7] Perez-Herrera, Rosa Ana, and Manuel Lopez-Amo. "Multi-Wavelength Fiber Lasers." IntechOpen, IntechOpen, 13 June 2013, www.intechopen.com/books/current-developments-in-optical-fiber-technology/multi-wavelength-fiber-lasers.

[8] "Optical Fiber Dispersion." Fosco Connect, www.fiberoptics4sale.com/blogs/archive-posts/95047942-optical-fiber-dispersion.

[9] S. Rashleigh, "Origins and control of polarization effects in single-mode fibers," in Journal of Lightwave Technology, vol. 1, no. 2, pp. 312-331, June 1983.

[10] Amari, Abdelkerim et al. "A Survey on Fiber Nonlinearity Compensation for 400 Gb/s and Beyond Optical Communication Systems." IEEE Communications Surveys & Tutorials 19 (2017): 3097-3113.

[11] CE Shannon, "A mathematical theory of communication," Bell system technical journal 27 (3), 379-423

[12] A. K. Srivastava et al., "Ultradense WDM transmission in L-band," in IEEE Photonics Technology Letters, vol. 12, no. 11, pp. 1570-1572, Nov. 2000, doi: 10.1109/68.887758.

[13] J. Tang, "The Shannon channel capacicty of dispersion-free optical fiber transmission," in Journal of Lightwave Technology, vol. 19, no. 8, pp. 1104-1109, Aug. 2001.

[14] G.P. Agrawal, "Fiber-Optic Communication Systems", 4th edn. John Wiley & Sons, New York, 2010.

[15] R. Dar, M. Feder, A. Mecozzi, and M. Shtaif, "Properties of nonlinear noise in long, dispersion-uncompensated fiber links," Opt. Express 21, 25685-25699 (2013).

[16] F. Forghieri, "Granularity in WDM networks: the role of fiber nonlinearities," IEEE Photon. Technol. Lett. 8(10), 1400–1402 (1996).

[17] A. Carena, G. Bosco, V. Curri, Y. Jiang, P. Poggiolini, and F. Forghieri, "EGN model of non-linear fiber propagation," Opt. Express 22, 16335-16362 (2014).

[18] L. Du and A. Lowery, "Optimizing the subcarrier granularity of coherent optical communications systems," Opt. Express 19, 8079-8084 (2011).

[19] M. Qiu, Q. Zhuge, M. Chagnon, Y. Gao, X. Xu, M. Morsy-Osman, and D. Plant, "Digital subcarrier multiplexing for fiber nonlinearity mitigation in coherent optical communication systems," Opt. Express 22, 18770-18777 (2014).

[20] A. Nespola et al., "Experimental demonstration of fiber nonlinearity mitigation in a WDM multi-subcarrier coherent optical system," 2015 European Conference on Optical Communication (ECOC), Valencia, 2015.

[21] A. Carbó, J. Renaudier, P. Tran, and G. Charlet, "Experimental Analysis of Non Linear Tolerance Dependency of Multicarrier Modulations versus Number of WDM Channels," in Optical Fiber Communication Conference, OSA Technical Digest (online) (Optical Society of America, 2016), paper Tu3A.6.

[22] P. Poggiolini et al., "Analytical and Experimental Results on System Maximum Reach Increase Through Symbol Rate Optimization," in Journal of Lightwave Technology, vol. 34, no. 8, pp. 1872-1885, 15 April15, 2016.

[23] P. Poggiolini, Y. Jiang, A. Carena, G. Bosco and F. Forghieri, "Analytical results on system maximum reach increase through symbol rate optimization," 2015 Optical Fiber Communications Conference and Exhibition (OFC), Los Angeles, CA, 2015, pp. 1-3, doi: 10.1364/OFC.2015.Th3D.6.

[24] R. Dar, M. Feder, A. Mecozzi, and M. Shtaif, "Accumulation of nonlinear interference noise in fiber-optic systems," Opt. Express 22, 14199-14211 (2014).

[25] F. Guiomar, A. Carena, G. Bosco, L. Bertignono, A. Nespola, and P. Poggiolini, "Nonlinear mitigation on subcarrier-multiplexed PM-16QAM optical systems," Opt. Express 25, 4298-4311 (2017).

[26] G. Raybon et al., "High Symbol Rate Coherent Optical Transmission Systems: 80 and 107 Gbaud," in Journal of Lightwave Technology, vol. 32, no. 4, pp. 824-831, Feb.15, 2014.

[27] A. Leven, N. Kaneda, U. Koc and Y. Chen, "Coherent Receivers for Practical Optical Communication Systems," OFC/NFOEC 2007 - 2007 Conference on Optical Fiber Communication and the National Fiber Optic Engineers Conference, Anaheim, CA, 2007.

[28] H. Meyr, M. Molenclaey, and S. Fechtel, "Digital Communication Receivers, Synchronization, Channel Estimation, and Signal Processing". John Wiley & Sons, New York, 1998, chapter 8.

[29] A. Leven, N. Kaneda, U. Koc and Y. Chen, "Frequency Estimation in Intradyne Reception," in IEEE Photonics Technology Letters, vol. 19, no. 6, pp. 366-368, March15, 2007.

[30] Ryan Ramdial, Xiaojun Liang, Shiva Kumar, John D. Downie, William A. Wood, "Frequency offset estimation algorithm for a multi-subcarrier coherent fiber optical system," Proc. SPIE 11309, Next-Generation Optical Communication: Components, Sub-Systems, and Systems IX, 113090K (31 January 2020).